

Modeling ultrafast magnetization processes in
3d-transition metals with an extension to the
Microscopic Three Temperature Model

Theodor Griepe

A thesis presented for the Degree of
Master of Science



Department of Physics

Freie Universität Berlin

03.01.2022

1st supervisor: Dr. Unai Atxitia Macizo

2nd supervisor: Prof. Dr. Martin Weinelt

Contents

1	Introduction	3
2	Background	5
2.1	Phenomenological models to describe UMD	6
2.1.1	The Three temperature model	6
2.1.2	Analytical expressions for 2TM-parameters	9
2.1.3	Landau-Lifshitz-Bloch equations	11
2.2	Microscopic Spin-flip processes	13
2.2.1	Elliot-Yafet mechanism	14
2.2.2	Electron phonon scattering (The M3TM)	16
2.2.3	Electron magnon scattering	25
2.2.4	Coulomb scattering	27
2.2.5	Electron-phonon spin flip probability	29
3	Methods	35
3.1	Simulation method	35
3.2	Influence of the M3TM-parameters on magnetization dynamics	36
3.2.1	Pulse parameters	38
3.2.2	Electron phonon coupling g_{ep}	41
3.2.3	Phonon specific heat c_p	42
3.2.4	Electron specific heat coefficient γ	44
3.2.5	Magnetization rate parameter R	44

<i>CONTENTS</i>	2
3.3 Ab initio parameters	46
3.4 Electron-spin energy transport	51
4 Results	56
4.1 Magnetization data on Iron, Nickel and Cobalt	57
4.1.1 Nickel	61
4.1.2 Iron	62
4.1.3 Cobalt	63
4.2 Data collected from Kerr rotation and ellipticity	64
5 Conclusion	69

Chapter 1

Introduction

Investigation of ultrafast magnetization dynamics has long been a hot topic of research with a high potential to significantly enhance the processing speed of magnetic memory devices while maintaining high precision. A broad variety of methods to manipulate magnetic properties of ferromagnets, antiferromagnets and ferrimagnets have been developed. To this end, interaction of photons and (anti)ferromagnets have been investigated in terms of the inverse Faraday effect, direct Zeeman coupling and thermal excitation by an optical pulse. The latter relates to the finding of Beaurepaire et al. in 1996, who could manipulate the magnetization of Nickel on a sub-picosecond timescale by irradiation with femtosecond optical laser pulses without application of an external magnetic field at room temperature [1]. Since the discovery of laser induced ultrafast magnetization dynamics (UMD) a theoretical explanation has been debated, with proposals ranging from spin transport phenomena into adjacent conducting substrates to different internal phenomena of angular momentum dissipation. This thesis aims to contribute to the debate, focusing on the description of internal phenomena, since the data set investigated in this thesis stems from experiments with non-conducting substrates. Understanding ultrafast magnetization dynamics from a theoretical standpoint will not only extend our knowledge of

solid state systems altogether but also help optimizing experimental methods in search for advanced memory devices. In chapter 2 some prominent models that have been proposed so far will be presented, starting with the phenomenological descriptions of the three temperature model (3TM) and the Landau-Lifshitz-Bloch (LLB) equations in sec. 2.1. Both of these link to the microscopic three temperature model (M3TM), introduced by Koopmans in 2008 [2], which will be used in this thesis upon proposing a small extension thereof to properly account for intrinsic energy flow. Besides the M3TM, which aims to explain loss of spin angular momentum due to spin flips upon electron-phonon scattering, also electron-magnon scattering [3] and Coulomb-scattering [4] have been proposed as leading mechanisms. The three theories have all shown reasonable agreement to experimental data, which will be discussed in sec. 2.2. The central matter of debate concerning the M3TM evolves around the probability of a spin flip upon an electron-phonon scattering event. By fitting the M3TM to experimental data with several fit parameters, Koopmans and co-workers determined the spin flip probabilities in iron and cobalt to be 15 – 20 [2]. Later on, ab initio calculations from Carva et al. suggested values an order of magnitude smaller [5]. A sketch of the approach for the ab initio calculations will be shown in sec. 2.2.5. In sec. 3.2 the influence of different parameters in the M3TM will be discussed. Ab initio parameters [6] for the electron and phonon temperature dynamics are implemented, as discussed in sec. 3.3. Thereby the set of free parameters is reduced to the spin flip probability and the absorbed pump power of the sample. It will be shown that only one parameter set can properly account for fixed magnetization dynamics. To properly account for the energy cost of spin flips throughout the dynamical process, an energy flow from electron to spin system is proposed in sec. 3.4, concluding the derivation of the extended M3TM. In chapter 4 some experimental data will be shown and fits with the extended M3TM will be discussed.

Chapter 2

Background

This section shall give a brief overview of the central matters of debate within theoretical models to describe ultrafast magnetization dynamics (UMD). First, the most relevant phenomenological models will be presented that are able to capture central features of UMD but lack insight into microscopic processes responsible for them. These include the three temperature model [1](sec. 2.1.1) and Landau Lifshitz Bloch equations [7] (sec. 2.1.3). Then three promising microscopic processes will be introduced that have been proposed to give a theoretical framework to explain experimental findings. The most prominent microscopic theories involve Elliott-Yafet (EY) processes. Central aspects of EY-mechanisms will be described in section 2.2.1. Most notably, the Microscopic Three temperature model, which is the central theory used in this thesis, will be introduced in section 2.2.2. Previous criticism of this model [5], evolving around the magnitude of spin flip probability upon electron-phonon-scattering events, is debated in sec. 2.2.5.

2.1 Phenomenological models to describe UMD

The very first theoretical model for ultrafast demagnetization was published with the first experimental observation thereof. UMD was first observed in Nickel in a seminal work conducted by Beaurepaire et al in 1996 [1]. Optical excitation of metals and metallic compounds with picosecond (ps)- and femtosecond (fs)- laser pulses was already a well established method to investigate phenomena such as electronic transport and superconductivity [8]. Experiments have shown that excitation and equilibration of electronic and phononic systems happen on a timescale of 1-10 ps, and their dynamics reveal direct insight into their coupling processes. Previous studies on spin dynamics on an ultrafast timescale have been conducted with ps- and ns-laser pulses. Agranat et al. used 5 – 20 ps pulses to heat their Nickel-sample and measured no demagnetization, concluding spin-electron and spin-lattice equilibration occur on a longer timescale [9].

Beaurepaire and co-workers argued that experiments conducted with a ps-time resolution are ill equipped to give insight to electron-spin and electron-lattice mechanisms on the fs-timescale. If spin-relaxation occurred on the same time scale as electrons and lattice relaxed, one would need a laser excitation in the fs-range to resolve magnetization dynamics. They thus used a laser pulse with temporal width of 60 fs to excite a Nickel sample and detect electron-, lattice- and spin-dynamics with a combination of transmittance spectra and MOKE measurements. Indeed, they were the first ones to publish a proof for magnetization dynamics on a fs-timescale (see fig. 2.1).

2.1.1 The Three temperature model

To describe the the dynamics of the three subsystems, Beaurepaire et al. assigned temperatures to them, thus implying thermal equilibrium within each system. The full description he used to fit the experimental results reads:

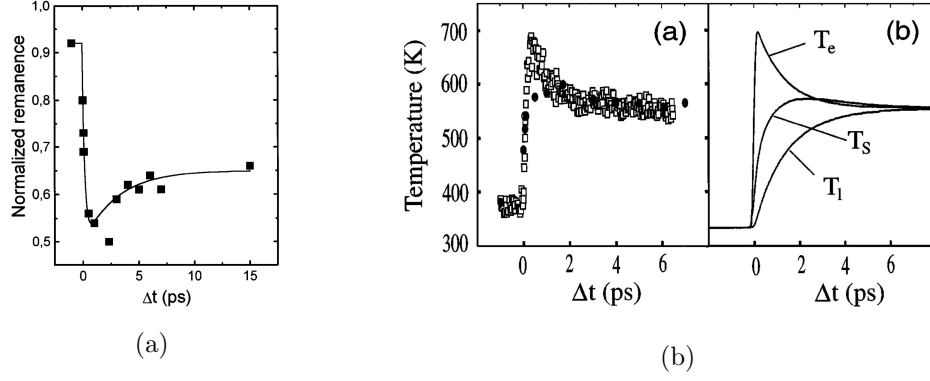


Figure 2.1: (a) Magnetization dynamics measured with MOKE. The magnetization drops to a minimum within the first 1 ps and remagnetizes on a timescale of ≈ 15 ps. (b) Temperature profiles deduced from experimental data (left, black dots show T_s , squares show T_e) and computed with the 3TM (right) (eqs. (2.1) - (2.3)). The electron temperature rises rapidly and relaxes through coupling with the other subsystems. It couples strongly to the spin system, which also increases rapidly after excitation. The phonon temperature couples mostly to the electron bath and increases steadily. The phenomenological model could reproduce the experimental data. *Both plots are reprinted from [1].*

$$C_e \partial_t T_e = -g_{ep}(T_e - T_p) - g_{es}(T_e - T_s) + P(t) \quad (2.1)$$

$$C_p \partial_t T_p = g_{ep}(T_e - T_p) - g_{ps}(T_p - T_s) \quad (2.2)$$

$$C_s \partial_t T_s = g_{es}(T_e - T_s) + g_{ps}(T_p - T_s) \quad (2.3)$$

$P(t)$ declares the power density of the incident laser pulse, that is absorbed only by the electron system. The energy is then distributed among the subsystems until temperatures equilibrate. Dependence on the spatial coordinates x, y, z is omitted here. z -dependence, declaring the depth in the sample, can be taken into account as the laser absorption is of exponentially decaying fashion. Dependence on the transversal coordinates x, y is usually

neglected, as samples are usually of smaller surface area than the excitation spot of the laser pulse. The sample is therefore heated homogeneously in good approximation. C_e , C_p and C_s declare the specific heat per volume for the electron, phonon and lattice system, respectively. The energies of each subsystem are determined by the product of specific heat and temperature CT in thermodynamic equilibrium. This implicitly assumes that the electronic, phononic and spin systems follow Fermi-Dirac, Bose-Einstein and Boltzmann statistics, respectively. Scattering events within each system are thus assumed to be much faster than inter-system-exchange processes. The dynamics of energy exchange between systems i, j are governed by a macroscopic coupling constant $g_{i,j}$. These coupling constants were taken as free parameters in Beaurepaire's simulation. Without detailing numerical values used in the fitting process, some phenomenological assessments can be deduced: To reproduce the magnetization curves of figures 2.1a and 2.1b(left), the following relations must hold:

$$C_s \ll C_p \quad (2.4)$$

$$g_{es} \gg g_{ps} \quad (2.5)$$

These relations guarantee that the spin system is more rapidly excited through coupling to the electrons than the phonon system. If $g_{es} \approx g_{ps}$, the magnetization would always lag electron-phonon dynamics, which contradicts experimental findings (see figure 2.1b (b) (b)). Furthermore, theoretical studies suggest that the spin system is far from thermal equilibrium within the first ≈ 1 ps after laser excitation and cannot be described adequately by a temperature T_s [10]. Thermalization of the electron system due to Coulomb scattering is also not instantaneous, but happens on a timescale of $\approx 100 - 300$ fs [2] [11]. The influence of non-thermal electron distributions on the magnetization dynamics will be discussed in section 2.2.5. Thus, new theories exploring the microscopic origins of ultrafast demagnetization concentrate on finding microscopical explanations for the coupling g_{es} . Many

models are based on the Two Temperature Model (2TM), which describes the dynamics of T_e and T_p without coupling to the spin system. Analytical expressions for the specific heats of electronic and lattice subsystems will be discussed in the next section.

2.1.2 Analytical expressions for 2TM-parameters

In the following, the specific heat of spins will be neglected, whereby equations (2.3) describe the Two-temperature-model (2TM), where only electrons and lattice are calculated and interact with each other. Within the model used in this thesis, the influence of spin specific heat is implicitly included by an energy-conserving term between electrons and spins (see section 3.4). With the assumptions on each subsystem mentioned in section 2.1.1 the electronic and lattice heat capacities can be computed analytically by defining the thermal energies ϵ of each subsystem. The derivation starts with the definition of Hamiltonians \mathcal{H}_e and \mathcal{H}_p . The electron system is described by a free electron gas, the phonon system is treated with the Debye-method:

$$\mathcal{H}_e = \sum_k E_k c_k^\dagger c_k \quad (2.6)$$

$$\mathcal{H}_p = \sum_q^{ND_p} \hbar\omega_q \left(\frac{1}{2} + a_q^\dagger a_q \right) \quad (2.7)$$

c_k^\dagger (c_k) creates (annihilates) an electron in state k in momentum space, E_k is the respective energy of said electron. The phonon system is described by ND_p quantum harmonic oscillators in state q , D_p being the number of polarisation states. $\hbar\omega_q/2$ is the ground state energy. The total thermal energies can be computed by integrating over all energies, weighed by the Density of states (DOS) and the temperature dependent distribution functions. They read

$$\epsilon_e(T_e) = 2 \int_0^\infty dE_e E_e f_e(E_e, T_e) D(E_e) \quad (2.8)$$

$$\epsilon_p(T_p) = \int_0^{E_D} dE_p E_p f_p(E_p, T_p) D(E_p), \quad (2.9)$$

where the phononic system is integrated up until the Debye-energy $E_D = k_B T_D$. The distribution functions read $f_e(E_e, T_e) = 1/(1 + \exp\{\frac{E_e}{k_B T_e}\})$ (Fermi-Dirac) and $f_p(E_p, T_p) = 1/(\exp\{\frac{E_p}{k_B T_p}\} - 1)$ (Bose-Einstein). The density of states of the electronic system depends on the band structure and is complex in general. However, only electrons near the Fermi-level contribute to scattering events, as the slope of the distribution function with respect to temperature is marginal for states far from Fermi level. The DOS can therefore be approximated by that at Fermi level, thus $D(E_e) = D_F$. The linearly dispersive phonons yield a density of states of $D(E_p) = 3N D_p E_p^2 / (k_B^3 T_D^3)$.

The specific heat of the electronic system can now be computed as [12]

$$\begin{aligned} C_e &= \partial_{T_e} \epsilon_e \\ &= \frac{1}{3} \pi^2 D_F k_B^2 T_e \\ &= \gamma T_e, \end{aligned} \quad (2.10)$$

so the electronic heat capacity increases linearly with electron temperature. The lattice heat capacity reads

$$\begin{aligned} C_p &= \partial_{T_p} \epsilon_p \\ &= \frac{3D_p}{Nk_B} \left(\frac{T_D}{T} \right)^3 \int_0^{\frac{T_D}{T}} du u^4 \frac{e^u}{(e^u - 1)^2}, \end{aligned} \quad (2.11)$$

where $u = \frac{E_p}{k_B T_p}$. The Debye-integral to compute the phonon specific heat cannot be computed analytically. For temperatures above T_D it asymptotically approaches a constant

$$C_p = Nk_B D_p, \quad (2.12)$$

which is often used to describe the phonon system of Nickel ($T_D \approx 477\text{K}$ [13]), since the phonon system in experiments at room temperature is rapidly increased to temperatures well above T_D after laser excitation. This approximation is not exact within the first 1ps, while the lattice is not heated above the Debye temperature.

2.1.3 Landau-Lifshitz-Bloch equations

One prominent model to give insight into possible mechanisms involved in demagnetization dynamics is the Landau-Lifshitz-Bloch (LLB) model. It describes the precession and relaxation of magnetization in presence of an effective magnetic field including coercive, external and thermally induced magnetic fields. The spin dynamics are described within a mean field model that is related to the atomistic Hamiltonian [6]

$$\mathcal{H} = \sum_{\langle i,j \rangle} J S_i S_j - d_z \sum_i S_z^2 \quad (2.13)$$

S_i denotes the spin at site i and J describes the mean field coupling between nearest neighbors. The second term describes the anisotropy with easy axes pointing along the z -axis. The LLB equation describes the dynamics of the macrospin $\mathbf{n} = \frac{\langle \mathbf{S} \rangle}{m_e(T)}$, normalized by the mean field equilibrium magnetization at temperature $T = T_e$. The temperature dynamics are usually computed via the two temperature model (see section 2.1.2). The LLB reads [14]

$$\partial_t \mathbf{n} = \gamma [\mathbf{n} \times \mathbf{H}_{\text{eff}}] - \frac{\gamma \alpha_{\perp}}{n^2} [\mathbf{n} \times [\mathbf{n} \times \mathbf{H}_{\text{eff}}]] + \frac{\gamma \alpha_{\parallel}}{n^2} [\mathbf{n} \cdot \mathbf{H}_{\text{eff}}] \mathbf{n} \quad (2.14)$$

$\gamma = \frac{g\mu_B}{\hbar}$ is the gyromagnetic ratio. As described by Atxitia et al. [7], the first term of equation (2.14) describes the precession of \mathbf{n} about the effective field

$$\mathbf{H}_{\text{eff}} = \mathbf{H}_{\text{int}} + \frac{m_e(T)}{2\chi_{\parallel}} (1 - n^2) \mathbf{n} \quad (2.15)$$

The effective field consists of contributions from Zeeman and anisotropy, magnetostatic interaction (contained in H_{int}) and a longitudinal field due to the thermal excitation of the exchange interaction, which is the dominant term in the presence of optical excitation. χ_{\parallel} is the material-dependent longitudinal susceptibility. The precession term is obtained by evaluating the time-dependent Schrödinger equation for the expectation value of spin $\langle \mathbf{S} \rangle$. The second term describes a transversal magnetization dissipation, also known as Gilbert damping.

Lastly, the final term describes the longitudinal relaxation of the magnetization and allows for a decrease in the length of the magnetization vector. The parameters α_{\perp} and α_{\parallel} are linked to the microscopic coupling parameter λ of lattice and electron systems, which basically reads the interaction matrix elements of lattice and electrons. They can be expressed as [7] [15]

$$\alpha_{\perp} = \frac{\lambda}{m_e} \left[\frac{\tanh(q_s)}{q_s} - \frac{T}{3T_C} \right] \quad (2.16)$$

$$\alpha_{\parallel} = \frac{2\lambda T}{3m_e T_C} \frac{2q_s}{\sinh(2q_s)}, \quad (2.17)$$

where $q_s = \frac{3k_B T_C m_e}{2(S+1)T_e}$. While precession and Gilbert damping can be expressed on an atomic scale for single spins, longitudinal damping is a prop-

erty of macrospin and can be connected to other models describing macroscopic magnetization dynamics, such as the M3TM. As mentioned above, the exchange field dominates the effective field upon laser excitation, as the electron temperature rises rapidly, thus driving the magnetization away from instantaneous equilibrium. Neglecting the contribution from H_{int} to the effective field, analogously to the derivation of M3TM, the longitudinal relaxation reads

$$\partial_t \mathbf{n}_{\parallel} = \frac{m_e \gamma \alpha_{\parallel}}{2\chi_{\parallel}} [1 - n^2] \mathbf{n} \quad (2.18)$$

It resembles the magnetization dynamics of the M3TM and both models can indeed be connected (see section 2.2.2).

2.2 Microscopic Spin-flip processes

The 3TM is a phenomenological theory relying on spin flip events within the magnetic sample to describe demagnetization. The coupling parameters g_{ep} , g_{es} and g_{ps} were introduced as fit parameters to achieve agreement with experimental data. As described in section 2.1, first results show that coupling of electrons and spins is the leading mechanism within this model. Different microscopical mechanisms contributing to this coupling have been proposed, such as the Microscopic Three Temperature Model (M3TM), which is used in this work. Other prominent models to describe demagnetization processes include spin transport phenomena and other spin flip theories. Spin transport phenomena can be suppressed by preparing the sample on non-magnetic insulating substrates, where neither charge nor spin currents can be transferred. Since the experimental data in sight of this thesis were collected under this condition, the theoretical discussion will focus on spin flip processes.

2.2.1 Elliot-Yafet mechanism

Models to describe spin flip processes within a coupling of electronic and spin systems rely on an Elloitt-Yafet type scattering event. This mechanism describes, how spin orbit coupling (SOC) can generate a spin flip, even if the respective interaction potential is spin diagonal. SOC induces electronic states, that are neither purely majority, nor minority states. Electronic states with momentum k in band n under the influence of SOC have a form [16]

$$\left| \Psi_{k,n}^{\uparrow} \right\rangle = a_{n,k}^{\uparrow} |\uparrow\rangle + b_{n,k}^{\uparrow} |\downarrow\rangle \quad (2.19)$$

$$\left| \Psi_{k,n}^{\downarrow} \right\rangle = a_{n,k}^{\downarrow} |\downarrow\rangle + b_{n,k}^{\downarrow} |\uparrow\rangle \quad (2.20)$$

$a_{n,k}^{\sigma}$ and $b_{n,k}^{\sigma}$ denote the k -dependent spin-correlation coefficients of electronic states in band n . In fig. 2.2 the band structure of Nickel along one axis in momentum space is shown, calculated by Kuch et al. [17]. Without detailing the different symmetries underlying the depicted bands, the figure visualizes eqs. (2.19) and (2.20). If it were not for SOC, majority and minority bands would run parallel and could be distinguished simply by their exchange coupling, where minority bands are higher in energy as majority bands (as denoted by the yellow marker). Spin-orbit interaction connects majority and minority bands, leading to a spin mixing within each band. In this situation, interband scattering can lead to loss of spin angular momentum through different spin configurations of initial and final state.

Starting with the band-resolved eigenstates (eqs. (2.19) and (2.20)), Elliott applied Fermis golden rule to find transition rates between different states [16]. He argues that any spin conserving transition is then proportional to the square of the matrix element

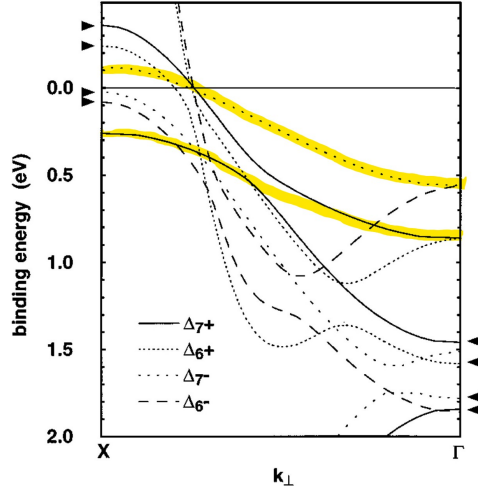


Figure 2.2: Relativistic electronic band structure of Nickel. SOC induces a band picture, in which majority and minority bands are ill defined. The yellow markerlines show majority (lower) and minority (upper) bands without SOC. They are simply split by exchange coupling, but contain only majority (minority) carriers. *Reprinted from [17]*

$$\int d\tau a_{k'}^* \mathcal{H}_{\text{int}} a_k e^{i(k-k')r} \quad (2.21)$$

and a spin-flip transitions will contain the square of

$$\int d\tau [a_{-k'} \mathcal{H}_{\text{int}} b_k - b_{-k'} \mathcal{H}_{\text{int}} a_k] e^{i(k-k')r}, \quad (2.22)$$

where $d\tau$ integrates over the unit cell. A more detailed discussion of golden rule transition rates will follow with the introduction to the Microscopic Three temperature model in section 2.2.2. Under the assumption of small-SOC-materials, where $a_k \gg b_k$, both being constant across the Brillouin zone (so neglecting degeneracies in the band model) and neglecting exchange splitting (investigating paramagnets), Elliott found that the integrals (2.22)

and (2.21) are in a constant ratio of $\frac{b_k}{a_k} = c$. Denoting the probability of a spin-flip (spin conserving) scattering as a_{sf} (a_{sc}) he concluded that

$$a_{\text{sf}} = c^2 a_{\text{sc}} \quad (2.23)$$

This relation was reformulated as the so-called Elliott relation to be [2] [18]

$$a_{\text{sf}} = p \langle b \rangle^2, \quad (2.24)$$

where $\langle b \rangle = \sum_n \int dk |b_n, k|^2$ is the expectation value of b and p is a material specific parameter, which ranges from $p \approx 1 - 10$ [2] [19]. The estimation of a_{sf} is a central part of this thesis and will be discussed repetitively. In chapter 2.2.5 critiques of this formalism in respect to its applicability to 3d-transition metals will be discussed, as well as different techniques to calculate this parameter.

The specifics of the physical origin of spin flip are contained in the interaction Hamiltonian \mathcal{H}_{int} . Arguably the most prominent candidate is an electron-phonon-scattering, because angular momentum conversation is explicitly taken into account through excitation of phonons, which act as a sink for angular momentum. Different theories have been employed in connection with an Elliott-Yafet like scattering process and will be discussed in more or less detail in the following sections.

2.2.2 Electron phonon scattering (The M3TM)

The Microscopic Three temperature model (M3TM), proposed by Koopmans et. al in 2009 [2], describes demagnetization in terms of phonon mediated spin flip processes. An electron's spin is flipped upon absorption or emission of a phonon. Importantly, this process explicitly accounts for

conservation of angular momentum, as the lattice acts as a sink of angular momentum. Furthermore, the appeal in this theory lies also within its computational simplicity. In this section I will describe the derivation of the Microscopic Three temperature model, as was presented by Koopmans [2].

Similarly to the 3TM (see section 2.1.1), the M3TM describes the dynamics of a ferromagnetic sample upon laser excitation in terms of three interacting subsystems, electrons, phonons and spins. The relevant Hamiltonians to describe the individual subsystems read

$$\mathcal{H}_e = \sum_k E_k c_k^\dagger c_k \quad (2.25)$$

$$\mathcal{H}_p = E_p \sum_q^{ND_p} \left(\frac{1}{2} + a_q^\dagger a_q \right) \quad (2.26)$$

$$\mathcal{H}_s = \Delta_{\text{ex}} \sum_j^{N_s} S_{z,j} \quad (2.27)$$

Equations (2.25) and (2.26) describe the energies of electron- and phonon systems, their dynamics are described by the two temperature model (see section 2.1.2). Note that to this point, the phonon system is described in the Einstein model, where all phonons contribute the same energy E_p . The electrons are considered spinless, the magnetic contribution is evaluated through assuming a lattice of localized spins at lattice sites $j = 1, \dots, N$. In mean field theory the exchange splitting of spin levels $S_{z,j}$ is (self-)dependent on the magnetization. For finite effective spin S of the system it reads

$$\Delta_{\text{ex}} = 3 \frac{S}{S+1} k_B T_C m, \quad (2.28)$$

where T_C denotes the Curie temperature of the system and k_B is the Boltzmann constant. To evaluate the dynamics of the subsystems, the interactions have to be taken into account. In the M3TM, three scattering processes

are considered. The exciting optical laser (pump) pulse induces spin conserving electric dipole transitions within the electron system [20], leading to a non-thermal electron distribution. The electron system thermalizes due to Coulomb scattering

$$\mathcal{H}_{ee} = \frac{U}{N^2} \sum_{k,k'} \sum_{k'',k'''} c_k^\dagger c_{k'}^\dagger c_{k''} c_{k'''} \quad (2.29)$$

This process is estimated to take $100 - 300$ fs [2] [11], shorter than all timescales of the ultrafast magnetization process. In this model, the Coulomb potential U is thus assumed infinite, whereby the electronic system can at all times be described by its temperature T_e . The electrons and phonons interact through scattering of the form

$$\mathcal{H}_{ep} = \sqrt{1 - a_{sf}} \frac{\lambda_{ep}}{N} \sum_{k,k'} \sum_q c_k^\dagger c_{k'} \left(a_q^\dagger + a_q \right), \quad (2.30)$$

where an electron in state k is scattered to state k' through emission (a_q^\dagger) or adsorption (a_q) for a phonon with momentum q . λ_{ep} denotes the strength of the electron-phonon interaction. In Koopmans' derivation, the spin flip probability a_{sf} is presumed to be sufficiently small, so that non spin-conserving scatterings do not influence the electron and phonon dynamics. Thus, e-p-scattering imposes a change on the phononic distribution f_p and can be calculated by applying Fermis Golden rule to Eq. (2.30), letting $a_{sf} = 0$ and integrating over all scattering events. Assuming a constant density of states D_F at Fermi level, the change in the phonon distribution upon emission or adsorption of a phonon with energy E_p reads

$$\begin{aligned} \dot{f}_p = \frac{2\pi}{\hbar} D_F^2 \lambda_{ep}^2 N D_p \left[(1 + f_p) \int d\epsilon (1 - f_e(\epsilon, T_e)) f_e(\epsilon + E_p, T_e) \right. \\ \left. + f_p \int d\epsilon (1 - f_e(\epsilon, T_e)) f_e(\epsilon - E_p, T_e) \right] \quad (2.31) \end{aligned}$$

The first term in Eq. (2.31) describes spontaneous (1) or stimulated (f_p) emission of a phonon in D_p equivalent polarisation states, the second term corresponds to adsorption of a phonon. $f_e(\epsilon \pm E_p, T_e)$ thus describes the available electronic states before scattering, $1 - f_e(\epsilon, T_e)$ denotes the occupied hole states to scatter into. Computing the integrals yields

$$\dot{f}_p = \frac{\pi}{\hbar} D_F^2 E_p \lambda_{\text{ep}}^2 \left[\coth\left(\frac{E_p}{2k_B T_e}\right) - \coth\left(\frac{E_p}{2k_B T_p}\right) \right] \quad (2.32)$$

The rate of energy transfer between electron and phonon systems can now be computed through the relation

$$\begin{aligned} \dot{\epsilon}_p &= \int dE_p D(E_p) E_p \dot{f}_p \\ &= \frac{3\pi D_F^2 D_P \lambda_{\text{ep}}^2}{\hbar E_D^3} \int dE_p E_p^4 \left[\coth\left(\frac{E_p}{2k_B T_e}\right) - \coth\left(\frac{E_p}{2k_B T_p}\right) \right], \end{aligned} \quad (2.33)$$

as only time evolution is only explicitly included in the occupation of phonon states f_p . E_D denotes the Debye energy. For $T_e, T_p \gg T_D$ this yields [21]

$$\begin{aligned} C_p \dot{T}_p &= \frac{3\pi D_F^2 D_P k_B E_D \lambda_{\text{ep}}^2}{2\hbar} (T_e - T_p) \\ &= g_{\text{ep}} (T_e - T_p) \end{aligned} \quad (2.34)$$

As mentioned before, spin flips are also induced by electron-phonon scatterings, where a localized spin is flipped with a probability a_{sf} upon scattering. The Hamiltonian reads

$$\mathcal{H}_{\text{eps}} = \sqrt{\frac{a_{\text{sf}}}{D_S}} \frac{\lambda_{\text{ep}}}{N^{3/2}} \sum_{k,k'} \sum_q^{ND_P} \sum_j^{N_S} c_k^\dagger c_{k'} (s_{j,+} + s_{j,-}) (a_q^\dagger + a_q), \quad (2.35)$$

where $D_S = N_S/N = \mu_{\text{at}}/\mu_B$ denotes the constant spin density at site j . The rate of spin flips can be computed in analogy to equation (2.32), where four different emission and adsorption processes have to be taken into account. The electron system can adsorb or emit phonons of energies $E_p \pm \Delta_{\text{ex}}$. To this end, the phonon system is treated in the Einstein model in Koopmans' derivation, meaning phonon frequencies lower than the maximum are neglected. Under the assumption $T_e, T_p \gg T_D$ and for spin $S = 1/2$ the spin rate reads

$$\dot{S} = -\frac{6\pi a_{\text{sf}} \lambda_{\text{ep}}^2 D_F^2 D_P k_B \Delta_{\text{ex}} T_p}{2\hbar E_D D_s} \left[1 + 2S \coth \left(\frac{\Delta_{\text{ex}}}{2k_B T_e} \right) \right] \quad (2.36)$$

Inserting Δ_{ex} (Eq. (2.28)), $S = -m/2$ and g_{ep} (eq. (2.34)) gives the rate of magnetization used to describe the magnetization dynamics within the M3TM (see below, Eq. 2.40).

So far, the treatment of electron and phonon temperatures (sec. 2.1.2) and thus of the magnetization dynamics were described for a uniformly excited sample. In reality however, a sample of finite depth absorbs the pump laser pulse non uniformly, the pump power decays exponentially into the sample. Due to the electrons' thermal conductivity κ , the arising temperature gradient creates thermal diffusion, which is captured by the continuity equation

$$\frac{dT_{e,\text{diff}}}{dt} = \nabla_z \kappa \nabla_z T_e. \quad (2.37)$$

Together with definitions of heat capacities (section 2.1.2) the dynamics of the three subsystems read

$$C_e \frac{dT_e(z, t)}{dt} = g_{e-p}(T_p - T_e) + \nabla_z \kappa \nabla_z T_e + S(z, t) \quad (2.38)$$

$$C_p \frac{dT_p(z, t)}{dt} = -g_{e-p}(T_p - T_e) \quad (2.39)$$

$$\frac{dm(z, t)}{dt} = Rm \frac{T_p}{T_C} \left(1 - \frac{m}{\tanh\left(\frac{\Delta_{ex}}{k_B T_e}\right)} \right), \quad (2.40)$$

where

$$R = \frac{8a_{sf}g_{ep}k_B T_C^2 V_{at}}{\mu_{at} E_D^2} \quad (2.41)$$

is the constant rate parameter. It scales inversely to the square of the Debye energy E_D , suggesting low frequency phononic excitations dominate spin flip events. Spin systems with lower atomic magnetic moment are more quickly disturbed. In case of 3d-transition metals, where orbital magnetic moments are quenched by the centrosymmetric crystal, the effective spin S is the main contribution to μ_{at} . R scales linearly with the rate of energy transfer g_{ep} between electron and phonon systems and the probability a_{sf} of a spin flip event upon such scattering event. Note that the magnetization will converge to $m_\infty = \tanh(\Delta_{ex}(m_\infty)/k_B T_\infty)$ after phonon- and electron temperatures have equilibrated at $T_\infty = T(t \rightarrow \infty)$, thus satisfying the Weiss mean field relation for the equilibrium magnetization at a given temperature.

Equation (2.40) holds for a spin $S = \frac{1}{2}$ system. Higher spin configurations, such as the high-spin phase in Iron with $S = 2$ [22] or Cobalt ($S = 3/2$ [23]) require a different treatment. The dynamics can be approximated by inserting the Brillouin function for different spin for the mean field equilibrium magnetization

$$\begin{aligned}
m_\infty &= B_S(m, T_e) \\
&= \frac{2S+1}{2S} \coth\left(\frac{2S+1}{2S} \frac{Jm}{k_B T_e}\right) - \frac{1}{2S} \coth\left(\frac{1}{2S} \frac{Jm}{k_B T_e}\right) \quad (2.42)
\end{aligned}$$

A more precise method was found by Beens et al. [24], who calculated the rates for all allowed transitions $\Delta m_S = \pm 1$ between the $2S + 1$ sublevels of the spin z component m_S . Again, this picture describes uncorrelated spins at each level m_S . The full spin description then reads

$$\frac{dm}{dt} = -\frac{1}{S} \sum_{m_s=-S}^{m_s=+S} m_s \frac{df_{m_s}}{dt} \quad (2.43)$$

$$\frac{df_{m_s}}{dt} = -(W_{m_s}^+ + W_{m_s}^-)f_{m_s} + W_{m_s-1}^+ f_{m_s-1} + W_{m_s+1}^- f_{m_s+1} \quad (2.44)$$

$$W_{m_s}^\pm = R \frac{Jm}{4Sk_B T_c} \frac{T_p}{T_c} \frac{e^{\mp \frac{Jm}{2Sk_B T_e}}}{\sinh(\frac{Jm}{2Sk_B T_e})} (S(S+1) - m_s(m_s \pm 1)), \quad (2.45)$$

where the change of occupation f_{m_s} of each spin level m_s is computed for each time step. The transition rates $W_{m_s}^\pm$ are computed from Fermis golden rule and for spin $S = \frac{1}{2}$ the set of equations reduces to equation (2.40).

Figure 2.3 shows experimental (dots) and simulated (solid lines) magnetization dynamics of a 15 nm Nickel thin film, irradiated with lasers of full width at half maximum (FWHM) of 50 fs and different fluences. Using $\frac{C_p}{\gamma}$, g_{ep} and P_0 as fit parameters Koopmans et al. extracted $a_{sf} \approx 0.19$ from the fitting process [2]. Comparing to ab initio calculations of $p \langle b^2 \rangle \approx 0.03 - 0.45$ as mentioned in section 2.2.1 they found agreement within the very broad range of ab initio predictions. The M3TM gives a convincing analytical framework to compute magnetization dynamics and indeed the same set of parameters could be used to match experimental data for different fluences. However, the magnitude of $a_{sf} \approx 0.19$ seemed unlikely large [25] [5] and is still a central matter of debate in this research field. A comprehensive

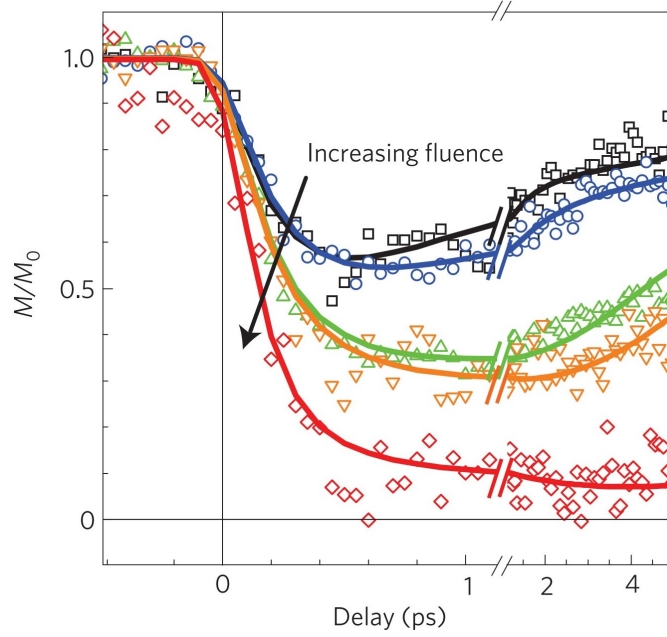


Figure 2.3: Magnetization dynamics of a 15 nm Nickel film, measured with MOKE technique and different pump laser fluences. The solid lines are simulated from equations (2.38)-(2.40) and various fitting parameters. Reprinted from [2]

study of the electron-phonon mediated spin flip probability by Carva et al. [5] using advanced ab initio calculations suggest that the values of a_{sf} for 3d ferromagnets are much smaller than those found by Koopmans, therefore suggesting that additional processes, such as spin currents are responsible for ultrafast demagnetization dynamics (see section 2.2.5).

Equivalence to Landau Lifshitz Bloch equations

From a more formal perspective, both the M3TM and the LLB models give macroscopic descriptions of magnetization dynamics upon laser excitation of a ferromagnetic sample. To recap, the LLB relations include terms for transversal and longitudinal relaxation, describing reorientation and disorder of the spin system, respectively. The M3TM considers a thermally

induced loss of order in the spin system and should therefor be linked to the longitudinal damping of the LLB. Such connection was derived by Atxitia et al. [7], where a more detailed description can be found. Starting from equation (2.40) and using the identity

$$B_{1/2}\left(\frac{T_C m}{T_e}\right) = \frac{2 \sinh\left(\frac{T_C m}{T_e}\right)}{B'_{1/2}\left(\frac{T_C m}{T_e}\right)} \quad (2.46)$$

the magnetization rate equation within the M3TM reads

$$\frac{dm}{dt} = -R \frac{T_p}{T_c} \frac{\mu_{\text{at}}}{k_B T_C} \left[\frac{2 \frac{T_C m}{T_e}}{\sinh\left(2 \frac{T_C m}{T_e}\right)} \right] \left(\frac{1 - \frac{B_{1/2}}{m}}{\mu_{\text{at}} \beta B'_{1/2}} \right) m. \quad (2.47)$$

Expanding $1 - \frac{B_{1/2}}{m}$ around m_e and m around m_e^2 (which is the leading term due to symmetry) yields

$$\frac{dm}{dt} = \frac{3R\mu_{\text{at}}}{2k_B T_C} \frac{2T_p}{3T_C} \frac{2 \frac{T_C}{T_e}}{\sinh\left(\frac{T_C}{T_e}\right)} m \left[\frac{1}{2\chi_{\parallel}} \left(1 - \frac{m^2}{m_e^2} \right) m \right]. \quad (2.48)$$

Comparing equations (2.48) and (2.18) one finds a link between the rate parameter R and the coupling factor λ within the LLB-description, where

$$\lambda = \frac{3R}{2\gamma} \frac{\mu_{\text{at}}}{k_B T_C} \frac{T_p}{T_e}, \quad (2.49)$$

showing that the M3TM can indeed be interpreted as longitudinal loss of spin angular momentum in the Landau Lifshitz Bloch equations.

2.2.3 Electron magnon scattering

In contrast to the M3TM, which is based on uncorrelated spin dynamics through electron-phonon scattering, Carpene et al. [3] proposed a spin flip mechanism based on electron-magnon scattering in 2008. Magnons are spin waves that can be excited through spin orbit interaction of the form

$$LS = L^+S^- + L^-S^+ + L_zS_z \quad (2.50)$$

In this sense, SOC-mediated processes can explain loss of spin angular momentum S through a subsequent gain in angular momentum L , described by the term L^+S^- of ladder operators. In terms of optically induced ultrafast demagnetization dynamics the argument goes as follows. Upon laser irradiation, electrons are excited to unoccupied levels and thermalize through Coulomb scattering, exchanging both linear and angular momentum. Treating the excitation within the electric dipole approximation, this process conserves spin angular momentum, so that in 3d ferromagnets minority states are significantly less occupied than majority states. Spin orbit coupling thus prefers spin flip scatterings of the form L^+S^- . Orbital angular momentum is quenched by a torque $T_z = -dU/d\phi$ exerted by the crystal field on electrons with potential energy U and rotation angle ϕ about the quantization axis z . As in the M3TM, the crystal field (lattice) acts as a sink for angular momentum. However in the demagnetization phase, magnons rather than phonons act as mediators of angular momentum. In Carpene's description, loss of angular momentum is assumed instantaneous, though it is mentioned that spin-orbit interaction implies only fractional quenching. The remagnetization phase is assumed to be driven by Elliott-Yafet type spin flips according to eq. (2.23). Comparing the dimensionless 'spin-mixing' parameter $c^2 (\approx 10^{-2} - 10^{-3}$ for other transition metals [26]) with with experimental fits yields broad agreement $\tau_s \approx 200 - 2000$ fs.

Figure 2.4 shows magnetization dynamics recorded on 7 nm Iron thin films

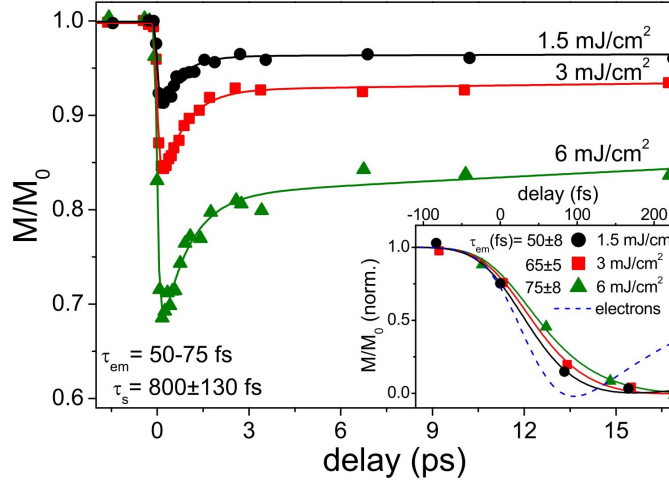


Figure 2.4: Magnetization dynamics of Iron upon irradiation of 60 fs laser pulses for different incident fluences, recorded by Carpenne et al. Demagnetization and remagnetization phase have been modeled with exponential functions including characteristic timescales τ_{em} and τ_{ep} . Reprinted from [3]

upon irradiation with 60 fs laser pulses for different fluences. The demagnetization phase was fitted with a function

$$m(t) = 1 - e^{-t/\tau_{em}} \quad (2.51)$$

while the remagnetization phase was modeled with biexponential fits representing spin relaxation on a fast time scale ($\tau_s \approx 1$ ps) and a slow thermal recovery time (> 100 ps). An analytical approach for calculating the electron-magnon equilibration time τ_{em} following the description of Allen [27] yields

$$\tau_{em} \approx \frac{5\pi k_B T_e}{3\hbar \lambda_m \omega_m^2} \approx 40 - 80 \text{ fs}, \quad (2.52)$$

matching the extracted fit values (see figure 2.4). Here, λ_m and ω_m denote

electron-magnon coupling constant (≈ 0.2) and magnon cutoff frequency, respectively.

In conclusion, electron-magnon scattering gives an intuitive low-energy description of a possible spin-flip mechanism. Although timescales for the quenching of orbital angular momentum (which also contributes to the magnetization) are excluded from the description proposed by Carpené et al., the extracted values for τ_{em} fit nicely to analytical estimates. Experimental X-ray magnetic circular dichroism (XMCD) measurements conducted by Boeglin et al. support the claim of spin and orbital angular momenta showing different dynamics on an ultrafast timescale in Cobalt [28].

2.2.4 Coulomb scattering

A third popular theory involving a spin flip mechanism is that of Elliott-Yafet Coulomb scattering. It was proposed by Krauss et al. in 2009 [4] and was supported by reasonable fits to experimental data, shown in figure 2.5a.

Krauss et al. also suppose spin-polarization conserving electric dipole transitions upon laser excitation of the electronic system, indicated by the vertical arrows in figure 2.5b connecting only majority (minority) bands respectively. The subsequent demagnetization is modeled by electron-electron scattering events from states ($|s_z, \text{momentum}\rangle$) $|\mu, k\rangle$ and $|\mu_2, l\rangle$ into states $|\mu_1, k + q\rangle$ and $|\mu_3, l - q\rangle$, respectively. The resulting screened Coulomb potential then reads

$$V_{\mu_2\mu_3}^{\mu\mu_1}(k, l, q, \omega) = \langle \mu, k | \mu_1, k + q \rangle \langle \mu_2, l | \mu_3, l - q \rangle v(q) \epsilon^{-1}(q, \omega), \quad (2.53)$$

where $v(q)$ denotes the bare Coulomb potential and $\epsilon(q, \omega)$ the Lindhard dielectric function, which contains screening effects at frequency ω and momentum q . Transition rates are then evaluated with Fermi's golden rule as

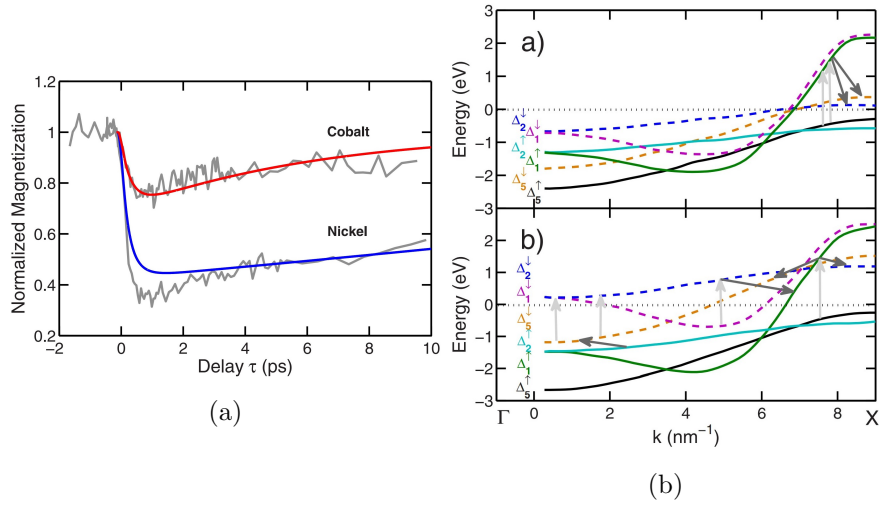


Figure 2.5: (a) Experimental data and simulations on magnetization dynamics in 15 nm Cobalt- and Nickel-films upon irradiation with 800 nm, 50 fs pump pulses. (b) Band structures in the vicinity of Fermi level centered at 0 of Nickel (top) and Cobalt (bottom) with excitation transitions (light grey arrows) and scattering transitions (dark grey arrows), from which interband transitions are deemed accountable for demagnetization. Reprinted from [4].

in the derivation of the M3TM, where e-e-scatterings are considered instead of e-p-scattering events. In an analogous fashion, spin transitions in Eq. (2.53) ($\mu \neq \mu'$) are considered with a momentum independent parameter α , whereas spin-conserving transitions are considered with a probability of 1. Krauss et al. modelled the remagnetization phase with thermal equilibration of electron and phonon systems, where loss of electronic energy leads to a redistribution into a spin-polarized arrangement. Fitting their simulations to experimental data on Nickel and Cobalt thin films (see Fig. 2.5a) they extracted fitting parameters $\alpha_{\text{Co}} \approx 0.15$ and $\alpha_{\text{Ni}} \approx 0.3$. These spin-flip probabilities are even higher than the ones proposed by Koopmans et al. [2]. However, scattering events of energetically equivalent electrons allow for a broader range of transitions in comparison to the quasi-elastic case of electron-phonon scattering, which makes possible a larger spin-flip probability. A shortcoming of this model is its lack of attention to angular momentum conservation, as the SOC-induced phonon dynamics would have to be taken into account for a proper description thereof.

2.2.5 Electron-phonon spin flip probability

The credibility of different theories of spin-flip interactions to explain ultrafast demagnetization lie within the reproducibility of experimental data, the completeness of their theoretical framework and good agreement of the used parameters to other experimental/theoretical studies. Regarding the reproducibility of experimental data, all of the above theories show promise. Especially the e-p- and e-e-scattering give complete numerical methods to simulate magnetization dynamics based on scattering interactions and Fermi's golden rule and can reproduce the characteristic features of ultrafast demagnetization nicely. While the theory of e-m-scattering does not provide a complete analytical or numerical framework, calculations of demagnetization times hint towards a possible agreement of theory and experiment. Regarding completeness, the M3TM is the most promising candidate, since it explicitly incorporates a sink for lost angular momentum upon demagne-

tization, a feature that both other theories fail to explain. It can explain both de-/ and remagnetization with the same process of electron-phonon scattering. While simplicity does not make the theory any more true than other candidates, it does make it easier to falsify. Within the well appreciated framework of Fermi's golden rule and basic quantum thermodynamics, magnetization can be computed by three simple differential equations. Parameters such as electron-phonon-coupling, heat capacities and atomic magnetic moment are established and well understood phenomena. Calculation of the spin flip probability within different scattering mechanisms is in principle understood. As for the Elliott-Yafet e-p-scattering, calculations conducted by Koopmans et al. [2] included several approximations and yielded a broad range ($a_{\text{sf}} \approx 0.03 - 0.45$ [2]), while direct experimental observation is impossible.

The spin flip probability found through Koopmans' fitting process seemed unlikely high and ab initio calculations were too imprecise to draw conclusions on it's usefulness. To shine light on this debate, Carva et al. proposed a more precise method to calculate a_{sf} from ab initio considerations [5]. Ab initio calculations from Koopmans determined the expectation value

$$\langle b^2 \rangle = \sum_{\sigma, n} \int dk |b_{k,n}^{\sigma}|^2 \delta(E_{k,n}^{\sigma} - E_F) \quad (2.54)$$

as mentioned in section 2.2.1 from band structures of Nickel and Cobalt. With equation (2.24) and $p \in [1, 10]$ this so-called Elliott relation inherits the following approximations: Variations of the electron-phonon matrix elements are small across the Brillouin zone, exchange splitting of majority and minority bands are neglected, b_k is constant and $a_k \gg b_k$ [5]. Especially the last three simplifications impair the value of calculations, since band crossing effects and significant band splitting (≈ 0.4 eV in Nickel [17], far greater than thermal smearing of several meV) are not respected in the simplified relation (2.24).

Carva et al. employed a method to explicitly calculate the electron-phonon matrix elements

$$g_{kn,k'n'}^{\nu\sigma\sigma'}(q) = \left| u_{q\nu} \langle \psi_{kn}^\sigma | \nabla_R V | \psi_{k'n'}^{\sigma'} \rangle \right|^2, \quad (2.55)$$

where $u_{q\nu}$ denotes the phonon mode of wave vector q in mode ν , $\nabla_R V$ is the gradient of the potential V felt by the electrons with respect displacement R of the atoms and ψ_{kn}^σ denote the wave functions defined in equations (2.19) and (2.20) [5]. Having defined electron-phonon matrix elements from the electronic wave functions one can define a spin flip energy-dependent Eliashberg function, which integrates Eq. (2.55) over all possible scattering partners at fixed energy and phonon frequency $\omega_{\nu q} = \Omega$:

$$\begin{aligned} \alpha_{\uparrow\downarrow}^2 F(E, \Omega) &\approx \frac{1}{2M|\Omega|} \sum_{\nu,n,n'} \int dk \int dk' g_{kn,k'n'}^{\nu\uparrow\downarrow}(q) \\ &\times \tilde{\delta}(E_{kn}^\uparrow - E) \tilde{\delta}(E_{kn}^\downarrow - E) \delta(\omega_{\nu q} - |\Omega|) \end{aligned} \quad (2.56)$$

Since the phonon excitation spectrum is energetically small compared to the electronic system, phonon adsorption and emission processes are considered in a broadened δ -function $\tilde{\delta}$ of width $2\hbar\omega_{\max}$ instead of explicitly requiring $\delta(E_{kn}^\sigma - E_{k'n'}^{\sigma'} - \hbar\Omega)$. Note that $\alpha_{\uparrow\downarrow}^2 F(E, \Omega) = \alpha_{\downarrow\uparrow}^2 F(E, \Omega) = \alpha_{sf}^2(F(E, \Omega))$ follows directly from the symmetry of Eq. (2.55). Finally, the transition rates are defined by integrating the Eliashberg function over all phonon frequencies. Note that emission and adsorption processes are included in (2.56) since the absolute value $|\Omega|$ is considered and the energy conservation conditions are described by broadened δ -functions. The transition rates then read

$$S^{+(-)} = \int dE \int_0^\infty d\Omega \alpha_{sf}^2 F(E, \Omega) [1 + 2f_p(\Omega)] f_e^{\downarrow(\uparrow)}(E) [1 - f_e^{\uparrow(\downarrow)}(E)] \quad (2.57)$$

and differ only in the occupation of majority (minority) electronic states $f_e^{\uparrow(\downarrow)}$. The probability of a spin flip at given distributions of electronic and phononic systems is then the total spin flip rate over the total scattering rate

$$a_{sf} = (S^+ + S^-) / \sum_{\sigma, \sigma'} S^{\sigma\sigma'}. \quad (2.58)$$

The spin flip probability cannot account for a change in magnetization if up-/ and down flips are equally probable, thus Carva et al. computed a second quantity, the demagnetization ratio

$$D_S = (S^- - S^+) / \sum_{\sigma\sigma'} S^{\sigma\sigma'}, \quad (2.59)$$

which gives insight into the actual demagnetization.

One major advantage of this formalism is its capability to investigate non equilibrium spin flip probabilities and demagnetization ratios by computing the e-p-scattering spin lifetimes

$$\tau_{sf}^\sigma(E) = n_\sigma(E) / w_{\uparrow\downarrow}(E), \quad (2.60)$$

where $w_{\uparrow\downarrow}(E) = d_E S^-$ denotes the spin transition rate at given electron energy E and $n_\sigma(E)$ are the number of states at the respective energy. This theoretical framework enables an investigation of the first few hundred fs

after pump pulse injection in which the electronic system is not thermalized due to Coulomb scattering. Table 2.1 shows results computed by Carva et al. from which two essential statements can be drawn: Firstly, the spin flip probabilities for Nickel and Cobalt extracted through the fitting process of Koopmans [2] are an order of magnitude higher than expected. Secondly, a non thermal electron distribution within the first few hundred fs is essential to observe noticeable demagnetization, as can be seen in the values of demagnetization ratios D_S . These findings suggest that non thermal electron distributions are deciding in achieving demagnetization due to optical excitation of 3d transition metals. As a consequence one could expect that the pulse duration itself plays a decisive role in the demagnetization phase, as the electron system takes longer to thermalize upon longer pulse excitation.

Material	temperature	a_{sf}	D_S
Nickel	low T	0.04	0
	3000 K	0.07	0.003
	non thermal	0.09	0.025
Iron	low T	0.04	0
	3000 K	0.09	0.008
	non thermal	0.07	0.03
Cobalt	low T	0.01	0
	3000 K	0.017	0.002
	non thermal	0.022	0.01

Table 2.1: Electron-phonon induced spin-flip probabilities a_{sf} and demagnetization ratios D_S computed by Carva et al. [5] for different materials, temperatures and non-thermal electron distributions. Low temperature calculations included a thermal smearing of 25 meV, maximum phonon frequencies of 35 meV and the transition rates were calculated for fixed electron energy at Fermi level. Most notably the results show that non thermal electron distributions are essential to achieve demagnetization even if spin flip probabilities are finite for all temperatures.

Chapter 3

Methods

Having introduced the theoretical concepts in the view of this thesis, the fitting process and details of the M3TM shall now be outlined. At first, the influence of different parameters within the M3TM on the magnetization dynamics will be discussed. Secondly, ab-initio-parameters for the temperature dynamics in the 2TM, provided by Zahn et al. [6], will be discussed and compared to the values used by Koopmans et al. [2]. The M3TM does not account for energy transfer between electron and spin system. In an attempt to account for an energetic cost of spin-flip events, an extension to the M3TM will be discussed in section 3.4.

3.1 Simulation method

The simulation was done using the python numpy package. The three differential equations (2.38), (2.39), (2.40) were computed iteratively for time steps of $\Delta t = 0.1$ fs. For each time increment, first the temperatures and then the magnetization were computed. The magnetization was set to saturation $m_0 = 1$ at the beginning of each simulation and was let to relax to its equilibrium at finite temperature before introducing the effect of the pump pulse. To achieve better computational convergence, the magnetization dy-

namics were computed with the Heun method, where

$$m(t_0 + dt) = m(t_0) + \frac{dm(t_0) + dm(t_0 + dt)}{2}, \quad (3.1)$$

where the increments dm are calculated according to Eq. (2.43). In the rest of this thesis, the laser pulse is assumed to cover the whole sample uniformly, thus lateral dependence is neglected. Differently, depth-dependence is respected by computing magnetization and temperatures for each layer in respective arrays of size according to the number of layers N in the sample. Including a heat transport-term and an exponentially decaying pump signal in the sample can lead to non-uniform temperatures and magnetization. For the computation of magnetization of systems with arbitrary spin $S > \frac{1}{2}$ (Fe, Co), an array of dimension $N \times (2S+1)$ holding the occupation f_{m_s} for each spin level at each site is saved after each iteration step. From this array, equations (2.43)-(2.45) can be readily computed.

3.2 Influence of the M3TM-parameters on magnetization dynamics

The M3TM can model ultrafast demagnetization in terms of inelastic scattering of electrons and phonons and subsequent spin flips. Figure 3.1 shows a simulation of electronic and phononic temperatures as well as magnetization, computed from equations 2.38-2.40 for a single layer sample with parameters Tab. 3.1. The dynamics can be explained as follows: The initially cold electron system has a low heat capacity ($C_e = \gamma T_e$), absorbs the pump pulse energy and thermalizes quickly. The electron temperature thus peaks right after laser excitation. Magnetic order is disrupted due to the electrons' heating and magnetization drops. Through electron-phonon scattering events the phononic system gets excited, thus phonon temperature rises and electron temperature drops until they equilibrate at a final temperature T_∞ . Because of the rapid increase in electron temperature,

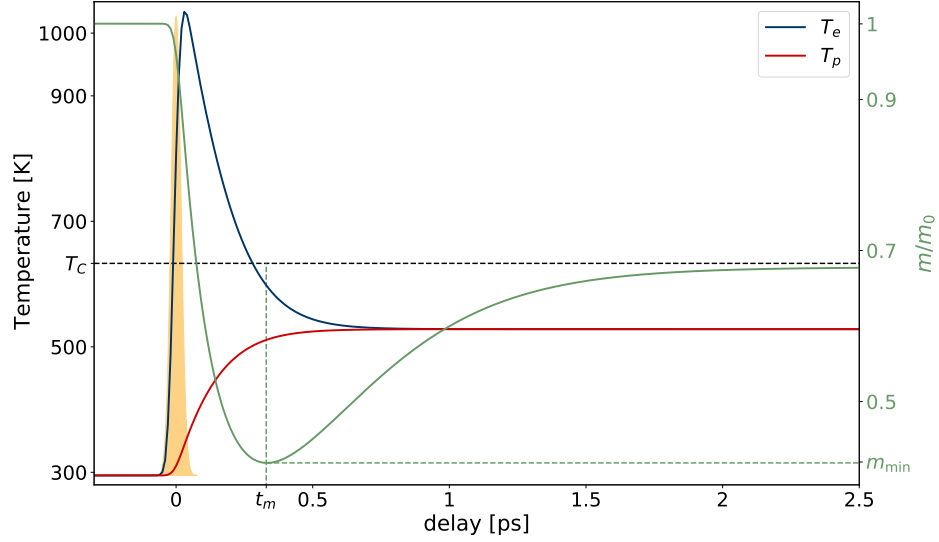


Figure 3.1: Simulated dynamics of the three subsystems in the Microscopic Three temperature model with parameters shown in Tab. 3.1 at room temperature. Electron temperature rises quickly upon absorption of the optical laser pulse (yellow) and equilibrates with the slowly reacting phonon temperature at a low temperature $T_\infty < T_C$. The magnetization drops to a minimum m_{\min} on a timescale of $t_m \approx 400$ fs (demagnetization phase) and remagnetizes on a longer timescale (Type I dynamics). The curve shows Type I behaviour here, because the demagnetization rate is sufficiently large to achieve $m < m_e(T_\infty)$ in this phase and the temperatures equilibrate at $T_\infty < T_C$.

Parameter	value	unit
Pulse width σ	18	fs
Peak pulse power density P_0	$14 \cdot 10^{21}$	$\frac{\text{W}}{\text{m}^3}$
electron specific heat γ	1000	$\frac{\text{J}}{\text{m}^3 \text{K}^2}$
phonon specific heat c_p	$2.3 \cdot 10^6$	$\frac{\text{J}}{\text{m}^3 \text{K}}$
electron phonon coupling g_{ep}	$4 \cdot 10^{18}$	$\frac{\text{W}}{\text{m}^3 \text{K}}$
magnetization rate parameter R	12	$\frac{1}{\text{ps}}$
Curie temperature T_C	633	K

Table 3.1: Magnetization parameters for the dynamics shown in figure 3.1. Throughout section 3.2 the dynamics illustrated in purple correspond to these parameters.

the spin system is thermally excited and the sample demagnetizes. After a time delay t_m the magnetization reaches its minimum m_{\min} of the demagnetization phase. If the demagnetization rate is sufficiently large so that $m(t_m) < m_e(T_e(t_m))$ and T_e , T_p equilibrate at a temperature $T_\infty < T_C$, magnetization will recover to $m_e(T_\infty)$ on a timescale of some picoseconds, which is called Type I behaviour. If $T_\infty > T_C$ magnetization will asymptotically approach $m = 0$ and if the demagnetization rate is small, m asymptotically drops to $m_\infty = m(T_\infty)$ once T_e and T_p have equilibrated (Type II behaviour). In its original publication the M3TM was shown to reproduce the transition of Type I and Type II behaviour very well. In the following, I will discuss the influence of material and experimental parameters on the simulation dynamics, which makes it possible to later understand experimental data of different materials in terms of different microscopic properties.

3.2.1 Pulse parameters

Experiments are often conducted with a pump pulse of Gaussian shape

$$P(t) = P_0 \exp\left(\frac{-t^2}{2\sigma^2}\right) \quad (3.2)$$

centered around a pump delay $\tau = 0$. The influence of the two parameters peak pump power density P_0 and variance σ will be discussed here.

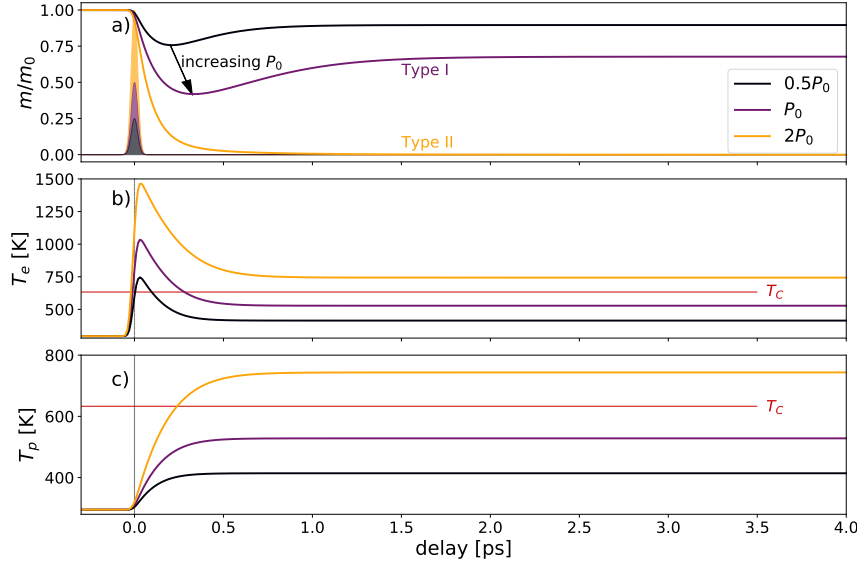


Figure 3.2: Dynamics of a) magnetization, b) electron temperature and c) phonon temperature for M3TM simulations computed with different parameters for the peak pump power density P_0 , as indicated by the pump profiles in a). For sufficient pump power $T_\infty > T_C$, Type II behaviour can be observed.

Figure 3.2 shows simulations conducted with different pump power densities P_0 . As all temperature and magnetization parameters are kept constant and the pulse shape is identical except for its height, the simulations are very similar. As more energy is absorbed by the electronic system for higher P_0 and the rate of energy exchange of electron and phonon system g_{ep} is constant, the overall timescale until equilibrium is increased with increasing pump power. This is reflected in the magnetization dynamics as well, as

indicated by the arrow in figure 3.2a). Upon increasing the peak pump power density, temperatures equilibrate at a higher T_∞ which translates to more disorder in the spin system and thus lower m_∞ . For sufficiently high pump powers T_∞ exceeds the Curie temperature T_C and magnetization asymptotically approaches $m = 0$ in Type II fashion.

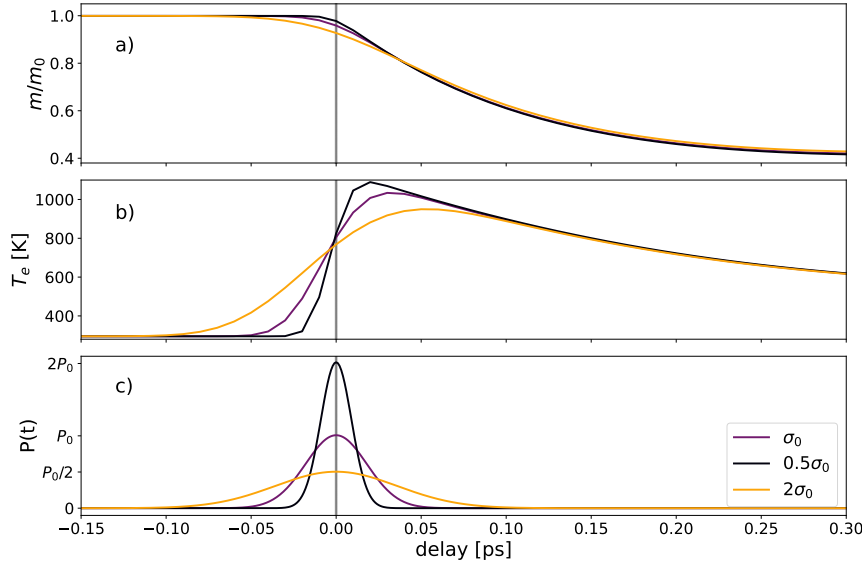


Figure 3.3: a) magnetization- b) electron- dynamics of M3TM simulations computed with different pulse widths, while conserving the overall absorbed energy. The different pulse shapes are shown in c). The electron dynamics clearly reflect the pulse shape. The magnetization, which reacts to the electronic response, is influenced around $t = 0$ and throughout the demagnetization phase. The pulse shape of an fs-laser pulse has no influence on the remagnetization phase.

The influence of different pulse widths σ as defined in Eq. (3.2) is shown in figure 3.3. Pump pulse power was normalized to yield the same absorbed energy density (integrated pulse) for all simulations. The strongest impact is detected by the electron system, which reacts directly to the shape of the injected pump pulse and resembles the pump shape. For large pulse widths

the temperature peak broadens. As discussed in section 2.1.1 the electron system does not thermalize instantly but is distributed non-thermally within the first 50 – 300 fs, depending on wavelength, power, duration and shape of the pump pulse. As the magnetization dynamics are moderately impacted by the pump shape throughout the demagnetization phase, slight variations in σ can be used to achieve better fitting results, as electron temperature is ill defined on this timescale.

3.2.2 Electron phonon coupling g_{ep}

The timescale of the overall magnetization process from laser excitation to magnetization equilibration is dominated by the electron-phonon coupling g_{ep} . Magnetization dynamics lag the electron temperature dynamics and are driven by electron phonon coupling. As long as $T_e > T_p$ the mean field magnetization $m_e(T_e)$ (Eq. (2.42)) continuously varies. Upon pump laser excitation the electron temperature rises quickly above T_c , which leads to disorder in the spin system and the magnetization drops. By coupling to the phonon system through the rate of energy transfer g_{ep} , T_e drops towards the equilibration temperature T_∞ , which is determined by γ , C_p and P_0 .

Figure 3.4 shows simulation dynamics for parameters shown in Table 3.1. Electron-phonon coupling is varied and the rate parameter R was adopted so that $\frac{R}{g_{ep}}$ is constant, since demagnetization is driven by electron-phonon-scattering and scales linearly in g_{ep} . The electron temperature rises higher from initial pulse excitation upon decreasing electron-phonon coupling, as the energy is more slowly distributed to the phonon system. It then approaches T_∞ more slowly as well. Magnetization dynamics are influenced similarly, as the rate R is diminished by decreasing g_{ep} . The demagnetization time until magnetization is fully quenched grows inversely proportional in g_{ep} , as indicated in figure 3.4a). Changing the electron-phonon rate conserves the final temperature and thus also equilibrium magnetization. Since the rate parameter R scales linearly in g_{ep} a transition from Type I to Type II behaviour cannot be achieved the adjustment thereof.

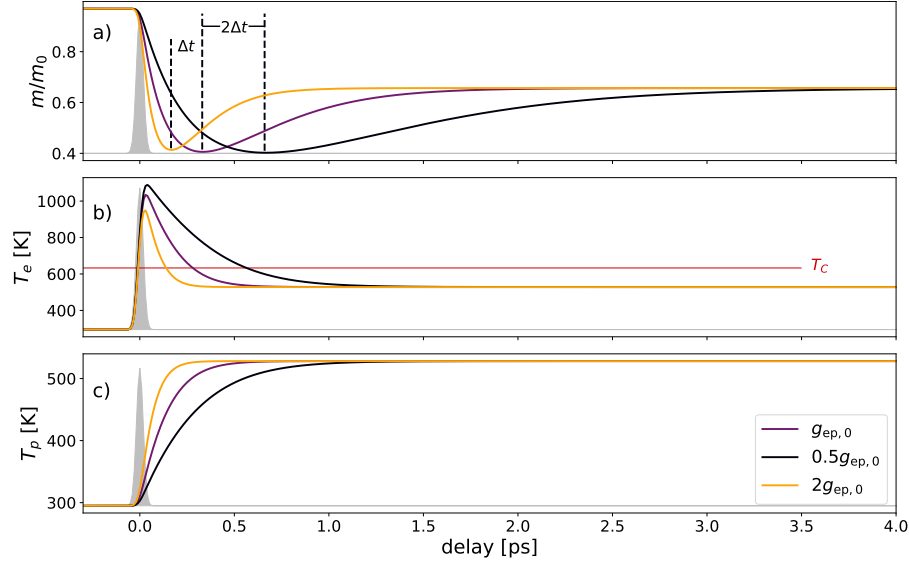


Figure 3.4: M3TM-dynamics of a) magnetization, b) electron temperature and c) phonon temperature with fixed parameters and varying values for g_{ep} , while the rate parameter $\frac{R}{g_{ep}}$ is constant for all three simulations. The profile of the pump pulse, centered at delay $t = 0$, is shown in grey shade. Magnetization dynamics are sped up by stronger electron-phonon coupling, while maximum magnetization quenching is hardly influenced and the equilibrium properties are exactly the same.

3.2.3 Phonon specific heat c_p

Since the rate of energy transfer between electron and phonon system is solely determined by g_{ep} , the temperature development is determined by the specific heats of each subsystem. By increasing phonon specific heat, T_p rises more quickly upon being excited by the heated electron system. Approximating UMD by instant heating of the electron system with linear specific heat ($C_e = \gamma T_e$) to a temperature $T_{e,0}$ and subsequent energy distribution to the phonon bath with constant specific heat at temperature $T_{p,0}$, T_∞ is determined by

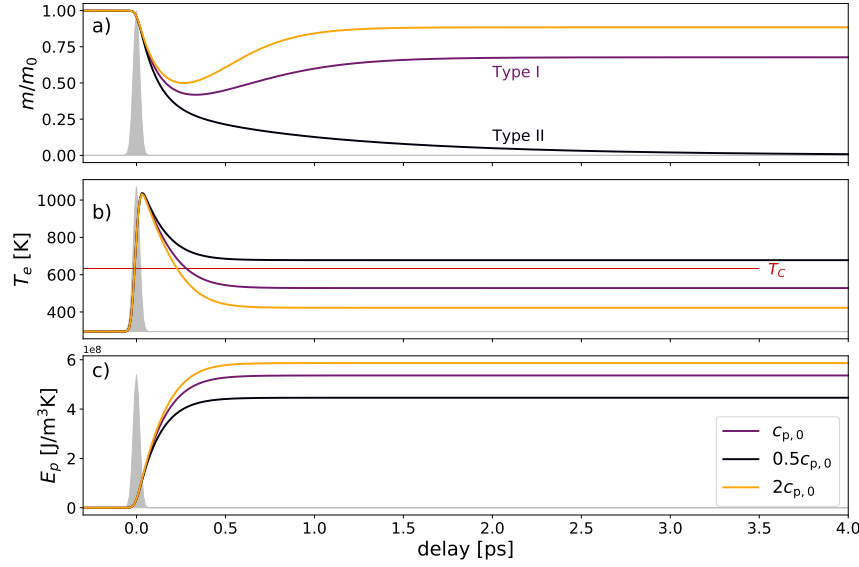


Figure 3.5: Dynamics of a) magnetization, b) electronic temperature and c) absorbed lattice energy density for M3TM simulations computed with different value for lattice specific heat C_p . The pump profile is sketched in grey, centered at delay $t = 0$. Equilibration temperature of electron and phonon systems rise with lower phonon specific heat, which leads to a lower equilibrium magnetization m_∞ . Type II dynamics can be observed for $T_\infty > T_C$.

$$C_p(T_{p,0} - T_\infty) = 2 [C_e(T_\infty)T_\infty - C_e(T_{e,0})T_{e,0}], \quad (3.3)$$

which can be found by integrating the two temperature model from $t = t_0$ at the moment of electron excitation to $t = t_\infty$ where electron and phonon temperatures have equilibrated. The factor 2 merely stems from integrating the left side of equation (2.38):

$$\int_{t_0}^{t_\infty} dt \gamma T_e \frac{dT_e}{dt} = [C_e(T_e) T_e]_{t_0}^{t_\infty} - \int_{t_0}^{t_\infty} dt \gamma T_e \frac{dT_e}{dt} \quad (3.4)$$

Figure 3.5 shows the dynamics of a) magnetization, b) electron temperature and c) absorbed energy density by the phonon system for varying lattice specific heats. Phonon specific heat does not influence the electron temperature peak after laser excitation. Energy is distributed between the two systems at a constant rate g_{ep} . The higher c_p , the more total energy will be transferred to the phonon system, so the equilibration process of the electron temperature takes slightly longer. The lower the phonon heat capacity, the higher its temperature will rise. The depth of the demagnetization peak is increased with increasing c_p , since the magnetization rate scales linearly in T_p . The most striking difference lies within m_∞ , which of course decreases with increasing T_∞ . For $T_\infty > T_C$, magnetization will not recover but asymptotically approach a totally disordered state $m = 0$ (Type II behaviour).

3.2.4 Electron specific heat coefficient γ

While varying phonon specific heat greatly influences T_∞ and m_∞ , electron specific heat has more impact on the absorption phase of the electronic system (see figure 3.6b)). For all simulations in figure 3.6 a constant amount of energy is absorbed, so that electron temperature rises higher the lower its specific heat. This translates to a larger response in the magnetization dynamics, since the thermal disorder in the spin system is more drastic the higher T_e rises. This leads to both a quicker and deeper demagnetization phase, as indicated by the arrow in figure 3.5c). Typically for experiments at room temperature $c_p \gg c_e$. Thus the equilibrium conditions are not influenced as much as through variation of c_p . To this end, increasing γ counteracts an increase in c_p (see figure 3.5). For sufficiently low γ , $T_\infty > T_C$ could be achieved and Type II dynamics would be observed.

3.2.5 Magnetization rate parameter R

The magnetization dynamics scale linearly in the rate parameter R , which includes microscopic parameters describing the reaction of the spin system

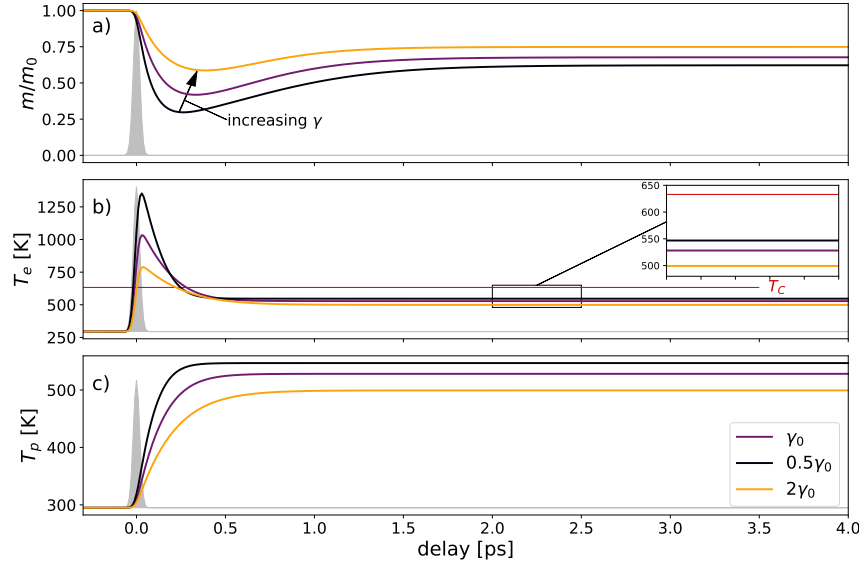


Figure 3.6: M3TM simulations for a) magnetization dynamics and electron (b) and phonon (c) temperature dynamics and different values for the electron specific heat coefficient γ . The pump profile is shown in grey shade. With decreasing γ , the electron temperature peaks higher upon pump absorption. Both the minimum magnetization m_{\min} and the delay of maximum quenching increases, as indicated by the arrow in figure a).

to scattering events of electrons and phonons (see Eq. (2.41)). Upon fixing the 2TM parameters such as c_p , E_D , γ and g_{ep} the elusive parameter of spin flip probability a_{sf} determines the magnitude of the rate parameter.

Figure 3.7 shows simulations conducted with different rate parameters R . In Koopmans' proposal of the M3TM [2] the specific heat of the spin system is neglected, so that magnetization dynamics have no influence on the temperature dynamics of electron and phonon system. Thus the two temperature model (Eqs. (2.38) and (2.39)) stays unchanged when altering R . Since magnetization recovery scales with the same dependence on R as the demagnetization and temperature dynamics are independent of the choice of R , the overall timescale until $m \rightarrow m_\infty$ is achieved stays constant. A

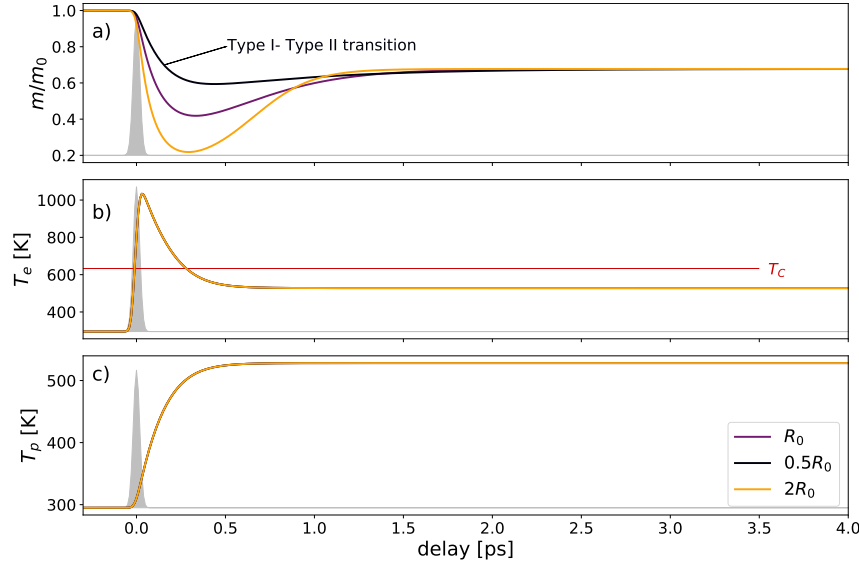


Figure 3.7: Magnetization (a) and temperature dynamics of b) electrons and c) phonons for different values of R . While electron and phonon temperature dynamics are not influenced by the rate of magnetization dynamics, the maximum magnetization quenching is increased by increasing R .

transition from Type I to Type II behaviour can be achieved by decreasing R and thus the response of the spin system to the temperature dynamics. For $R = 0.5R_0$ the magnetization dynamics transition from Type I to type II behaviour (Fig. 3.7a).

3.3 Ab initio parameters

As shown in the previous section, the fitting process is complicated and tedious, if all mentioned parameters are treated as free parameters. Several constellations of parameters can yield very similar results. Upon introducing the M3TM, Koopmans and co-workers fitted experimental data with g_{ep} , R , $\frac{C_p}{\gamma}$ and P_0 ¹ as free parameters [2]. In summary, the latter three parameters all influence the depth of the demagnetization phase, while the

latter two determine the equilibrium magnetization m_∞ . In order to extract the spin flip probability from simulations, fits should have a unique parameter set best suited to fit experimental data. Indeed, this can only be achieved by reducing the set of free parameters. Using temperature dependent ab initio parameters for the specific heats and electron-phonon coupling leaves only the magnetization rate R (and thus a_{sf}) and pump power P_0 to be adjusted. As varying the magnetization rate has no effect on m_∞ , there exists a unique combination of the two parameters that can replicate both the depth of demagnetization peak and equilibrium magnetization. In the following, ab initio parameters for g_{ep} , C_p and γ will be discussed and compared to the parameters used by Koopmans [2]. The data was kindly provided by Zahn et al. [6], published in an investigation of phonon dynamics in 3d ferromagnets upon ultrafast laser excitation.

Koopmans determined the ratio of $\frac{C_p}{\gamma}$ by fitting phonon specific heat to experimental magnetization dynamics data and adjusting electron specific heat, so that

$$C_e(T = 300 \text{ K}) + C_p = C(T = 300 \text{ K}). \quad (3.5)$$

Resulting values for γ in Nickel (Cobalt) of 5435 (5533) $\frac{\text{J}}{\text{K}^2\text{m}^3}$ are shown in figure 3.8 and deviate significantly from ab initio calculations and literature values of $\gamma \approx 1000 \frac{\text{J}}{\text{K}^2\text{m}^3}$ [29] [30] [6].

Figure 3.9 shows temperature dependent phononic heat capacities for Iron, Nickel and Cobalt from ab initio calculations [6] in comparison to values used by Koopmans et al. [2]. Ab initio calculations show a temperature dependence reminiscent of the Debye model, yielding very good agreement to experimental data collected by Meschter et al. [30]. As can be seen

¹As can be seen in figure 2.3, Koopmans fitted a set of curves for different fluences, thus the pump power P_0 was not treated as a truly *free* parameter, the ratios of absorbed pump energies of different magnetization curves reflects the ratios of laser fluences, which can be determined experimentally.

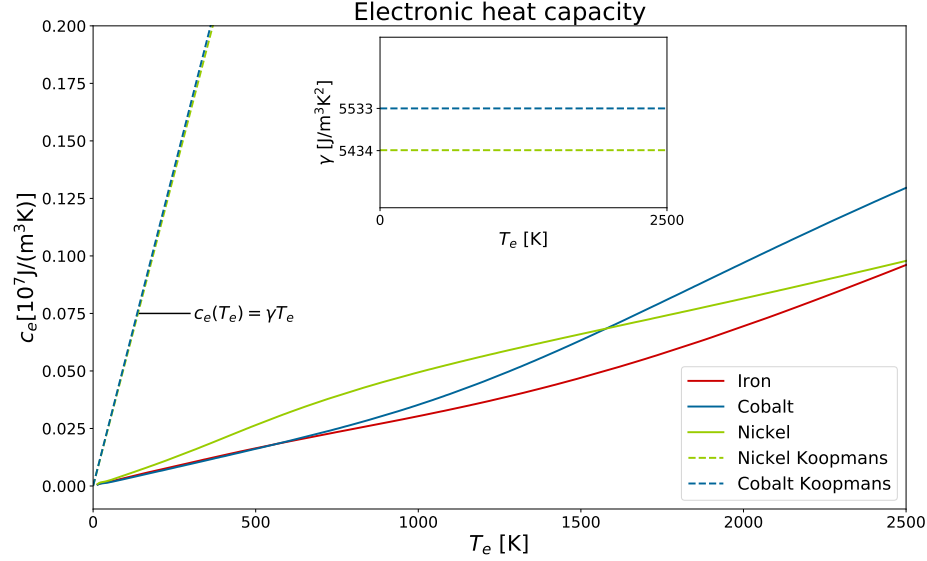


Figure 3.8: Electronic heat capacities for Iron, Nickel and Cobalt from ab initio calculations [6] (solid) and values used by Koopmans [2] (dashed). While Koopmans used the analytical approximation outlined in section 2.1.2, ab initio calculations show slight deviations from strictly linear behaviour. The slope of c_e used by Koopmans is more than 5 times higher than predicted by ab initio calculations.

in sections 3.2.4 and 3.2.3, a decrease in γ requires higher c_p in order to conserve T_∞ and thus m_∞ . The lower the electronic specific heat, the higher T_e will rise due to laser excitation. Within this model this results in a larger demagnetization even if the rate parameter is kept constant, since magnetization is driven towards a lower equilibrium value $m(T_e)$. Thus decreasing the spin flip probability a_{sf} replicates magnetization dynamics with higher electronic heat capacity well.

Figure 3.10 shows ab initio calculations for the electron-phonon coupling g_{ep} for Iron, Nickel and Cobalt in comparison to values used by Koopmans [2]. While Koopmans fixed a constant value for g_{ep} , as suggested by the analytical approach outlined in 2.2.2, ab initio calculations for electron phonon

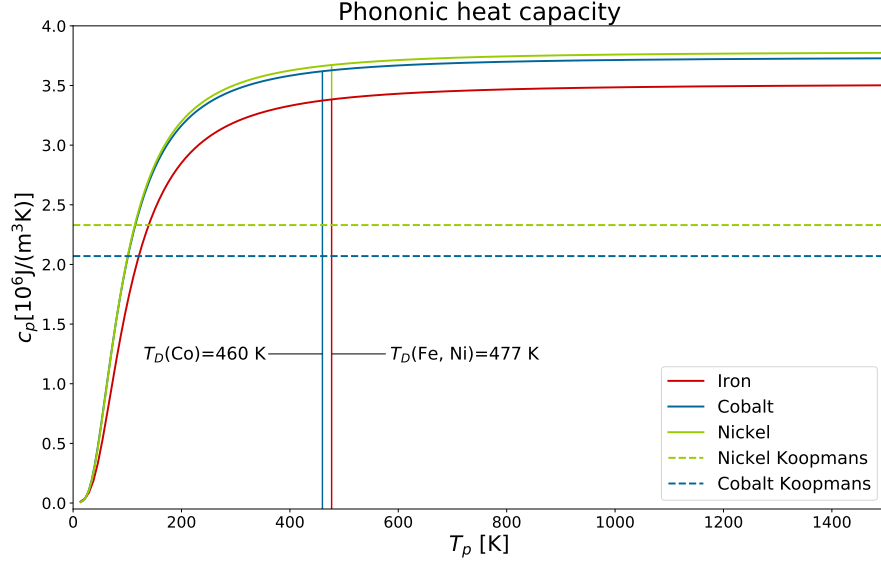


Figure 3.9: Lattice heat capacities from ab initio calculations [6] (solid) and values used by Koopmans [2] (dashed). While Koopmans used constant values, ab initio calculations show a temperature dependence similar to the Debye model. For temperatures above the respective Debye temperatures T_D , the lattice heat capacities approach a constant value, larger than the ones obtained in the fitting process of Koopmans

coupling reflect the behaviour electronic and lattice heat capacities. For low temperatures, g_{ep} rises quickly due to the increase in c_p . As c_p stagnates for temperatures above T_D , the temperature dependence of g_{ep} shares features of the electronic heat capacities. While the slope of $c_e(\text{Ni})$ decreases for $T_e > 1000 \text{ K}$, $g_{\text{ep}}(\text{Ni})$ decreases as well. In this regime, γ and g_{ep} of Iron and Cobalt are increased.

Values for g_{ep} in literature deviate significantly. While values used by Koopmans are roughly a factor of two higher, while there are also reports of g_{ep} being an order of magnitude smaller than calculated by Vorberger et al. [6]. Although the rate of energy flow between electron and phonon systems

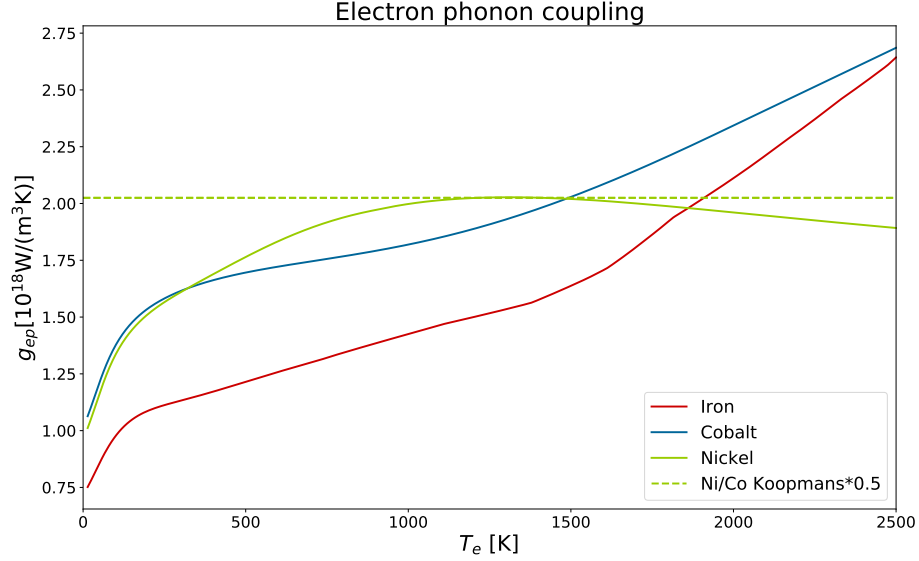


Figure 3.10: Comparison of electron-phonon-coupling in Fe, Ni, Co from ab initio calculations [6] and constant values used by Koopmans [2]. Values obtained in the fitting process by Koopmans are significantly higher than ab initio predictions.

is essential in determining magnetization dynamics within the M3TM, g_{ep} does not influence the depth of the demagnetization peak and thus does not interfere with the choice of the spin flip probability (see sections 3.2.2 and 3.2.5). The rate of energy transfer shown in figure 3.10 was computed for spin conserving electronic transitions only. Thus, to adequately account for energy flow between the three subsystems of electrons, phonons and spins, an energy cost for spin excitations must be accounted for. In an attempt to do so, an extension to the temperature dynamics within the M3TM will be discussed in the following section.

3.4 Electron-spin energy transport

The previous section concludes the study of the influence of the parameters within the original Microscopic Three Temperature Model on simulated temperature and magnetization dynamics. Subsection 3.2.5 clarifies that the magnetization dynamics have no effect on electron and lattice systems, which is due to the neglect of spin specific heat, i.e. thermal energy stored in the spin system. Indeed, defining spin specific heat on ultrafast timescales is problematic since a true spin temperature, as proposed in the Three Temperature Model (see section 2.1.1), is ill defined since the spin system is not in internal equilibrium. However, thermal energy stored within the spin system should not be disregarded. Recently, Jacobs et al. proposed a method to incorporate spin energy in atomistic spin dynamics (ASD) simulations [6]. In their ASD simulations, thermal disorder in the spin system is driven by Gaussian white noise that scales linearly in electron temperature, which is determined by the Two Temperature Model. By deducting the increment of Heisenberg energies from the thermal electronic energy after each time step, they were able to reproduce very nicely the experimental data on lattice dynamics in Nickel upon ultrafast laser excitation. In a similar attempt, the M3TM can be extended by introducing a new term to the electron dynamics:

$$C_e \frac{dT_e}{dt} = -g_{ep}(T_e - T_p) - \frac{dQ_{e-s}}{dt}, \quad (3.6)$$

where the last term corresponds to the increment of mean field Heisenberg energy

$$\frac{dQ_{e-s}}{dt} = Jm \frac{dm}{dt}. \quad (3.7)$$

Figure 3.11 sketches the energy flow in the demagnetization and remagnetization phases upon including Eq. 3.7 to the electron temperature dynamics.

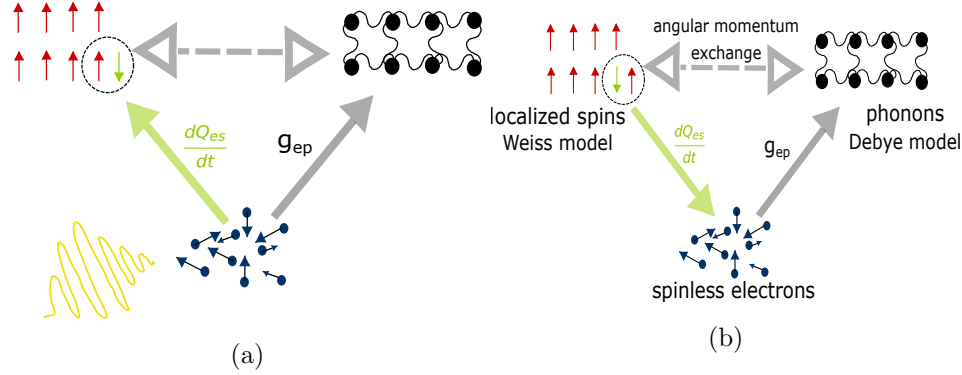


Figure 3.11: (a) Energy and angular momentum flow in the extended M3TM during the demagnetization phase. Energy is absorbed from the pump pulse by the electron system and distributed to phonons and spins, which exchange angular momentum during spin flip events. (b) In the remagnetization phase, thermal energy is fed back from the spin system to the electron system due to realignment of spins. The electron temperature thus stays above the lattice temperature and energy flows indirectly from the spin system to the phonon system.

Fig. 3.12 shows the influence on magnetization and energy dynamics of each subsystem. Magnetization dynamics within the a) original and b) extended M3TM are shown in the bottom figure. Most notably, the extended M3TM predicts a higher final magnetization upon absorption of the same pump energy. This corresponds to a lower equilibration temperature of electronic and lattice subsystems. The reason for this can be seen in the top figures, which show the dynamics of absorbed energies in each subsystem in the two simulations. The total absorbed energy

$$E_{\text{tot}}(t) = \int^t d\tau P(\tau) \quad (3.8)$$

$$= \int^t d\tau (E_e(\tau) + E_p(\tau) + E_s(\tau)) \quad (3.9)$$

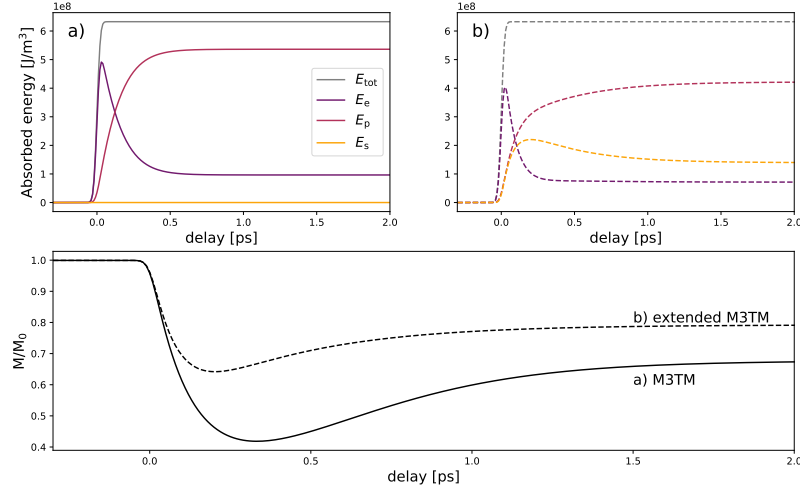


Figure 3.12: Bottom: Normalized magnetization dynamics computed with parameters listed in Tab. 3.1 and a) M3TM and b) extended M3TM including an energy flow between electron and spin systems (Eq. 3.7). Top: Corresponding absorbed total energies (E_{tot}) and energy dynamics of electronic (E_e), phononic (E_p) and spin (E_s) subsystems, both following the same color coding. Although the same energy is absorbed from the pump pulse, electron and phonon systems absorb less energy due to the consideration of the energetic cost of thermal spin disorder.

behaves exactly the same in both simulations. In the M3TM (a) the total energy is distributed among electronic and lattice subsystems only while no energy cost is accounted to disorder in the spin system. In the extended model (b) the spin system absorbs a finite energy $E_s(t) = \int^t d\tau \frac{dQ_{e-s}}{d\tau}$, influencing both electron and phonon dynamics.

The absorbed electron energy E_e does not peak as high due to the spin system absorbing energy right away. Magnetization still drops after the laser pulse has been fully absorbed by the electron system, leading to a quicker

equilibration of electron temperature/ energy due to the energy flow from the electron system to the spin system. Due to the low specific heat of the electron system, the final absorbed energy does not deviate much from simulations with the original M3TM.

The lattice dynamics significantly slow down once the sample remagnetizes and the electron temperature has equilibrated. The subsequent slow rise of phonon energy is due to the recovery of magnetization. While electron temperature and energy stay approximately constant, energy is indirectly distributed from the spin system to the lattice. Due to its high heat capacity, the difference in equilibrium phonon energies deviate drastically between the two models.

To fit the extended M3TM to the same data as the conventional method under the restrictions to parameter changes listed in section 3.3, both peak pump power density P_0 and the magnetization rate parameter R have to be adjusted to fit the final magnetization m_∞ and the depth of the magnetization peak. Following the argument above, pump power must be increased to match the final magnetization. Due to the electron temperature decreasing more quickly after excitation, the magnetization is not quenched as much, even if P_0 is increased to match m_∞ . Thus, increasing R according to table 3.2 yields the simulation shown in figure 3.13. Magnetization dynamics are faster since T_e equilibrates quicker and m strives towards $m_e(T_e)$ at any time. To this end the energy transfer term \dot{Q}_{e-s} has a similar effect on the magnetization dynamics as increased electron-phonon coupling if R and P_0 are treated as free parameters.

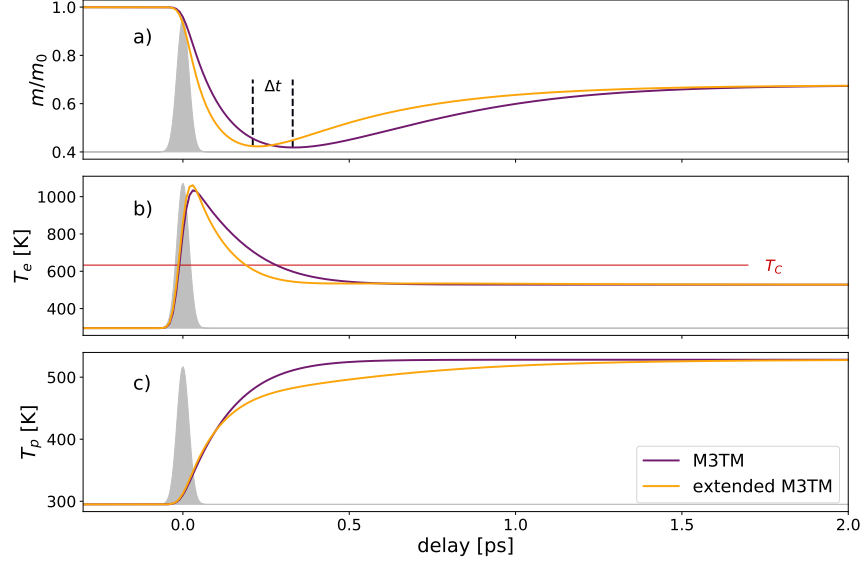


Figure 3.13: Exemplary plot on how the M3TM and the extended M3TM can be fitted to the same data with only P_0 and R treated as free parameters. The choices for both parameters are shown in table 3.2. The electron temperature (b) drops more quickly due to an energy flow from electron- to spin- system and thus the magnetization dynamics (a) are sped up upon including an energy flow between electron- and spin subsystems. The lattice dynamics are slowed down in the remagnetization phase, since the electron temperature has already approached T_∞ due to the energy flow to the spin system.

	P_0 [$10^{21} \frac{\text{W}}{\text{m}^3}$]	R [$\frac{1}{\text{ps}}$]
M3TM	14	12
extended M3TM	18.5	17

Table 3.2: Comparison of parameters used in figure 3.13. All other parameters are listed in Tab. 3.1.

Chapter 4

Results

In this section, different experimental data on ultrafast magnetization dynamics in 3d ferromagnets will be discussed and simulated magnetization dynamics with the extended M3TM will be fit to this data. 3d transition magnets show a simple band structure around the Fermi edge and the magnetic moment is almost purely generated by itinerant electrons in the 3d band. This allows for simplification of magnetic behaviour in terms of a localized spin subsystem. With the fitting process outlined in the methods section, a value for the spin flip probability can be extracted for each data set, as ab initio parameters for γ , C_p and g_{ep} are fixed in the simulations, leaving only the pump power density and spin flip probability as free parameters.

Two different data sets are to be discussed in this thesis. The first one shows magnetization dynamics for Iron, Nickel and Cobalt taken under the same conditions for a variety of pump fluences, recorded by Borchert et al. [31] at the Max-Born Institute Berlin. A second data set was provided by Checkhov et al. [32] at the FU Berlin and shows not only the magnetization dynamics but also raw experimental data of MOKE rotation and ellipticity. It will be discussed how treatment of the data influences the retrieved magnetization

dynamics and agreement of simulation and experiment.

4.1 Magnetization data on Iron, Nickel and Cobalt

The first data set to be discussed was recorded by Borchert et al. [31]. Magnetization dynamics on in plane magnetized thin films (15 nm) of Iron, Nickel and Cobalt were recorded by longitudinal MOKE measurements at room temperature in a pump ($\lambda_{\text{pump}} = 800$ nm) probe ($\lambda_{\text{probe}} = 400$ nm) setup. Magnetization dynamics were retrieved by toggling an external magnetic field and collecting the difference spectra of the transient MOKE signals. Through separating s- and p- components of the probe beam and determining their difference spectra, a signal proportional to the Kerr rotation and thus magnetization were retrieved. Insulating glass wafers were used as substrate, suppressing any effects of spin transport phenomena between sample and substrate. Thus the change in magnetization upon laser excitation must be dominated by internal phenomena, i.e. spin-flip events. Samples were capped with 2 nm of Ta to prevent oxidation, however the influence of the small cap was not investigated experimentally and will be neglected within this analysis.

Data was collected for a set of different incident pump fluences $F_{i,\text{exp}}$ and a Gaussian pump laser of constant FWHM of 39 fs, which corresponds to $\sigma = 17$ fs. As incident pump laser fluence, absorbed pump power and peak pump power density P_0 are proportional, the ratio of incident fluences should be reflected in the ratio of the parameters P_0 for different curves. This holds true as long as incident laser fluences do not exceed the materials damage thresholds. The range of fluences used in the experiment are shown in Tab. 4.1. While there is no data on damage thresholds in Iron and Cobalt, the limits are not exceeded for Nickel [33]. To determine the absorbed fluence in simulations, the penetration depth of the laser is estimated. It is stated that a few percent of the incident fluence was transmitted through the sample. Assuming no absorption of the substrate and exponentially decaying absorption through cap and sample with 5 percent transmission ($t = 0.05$)

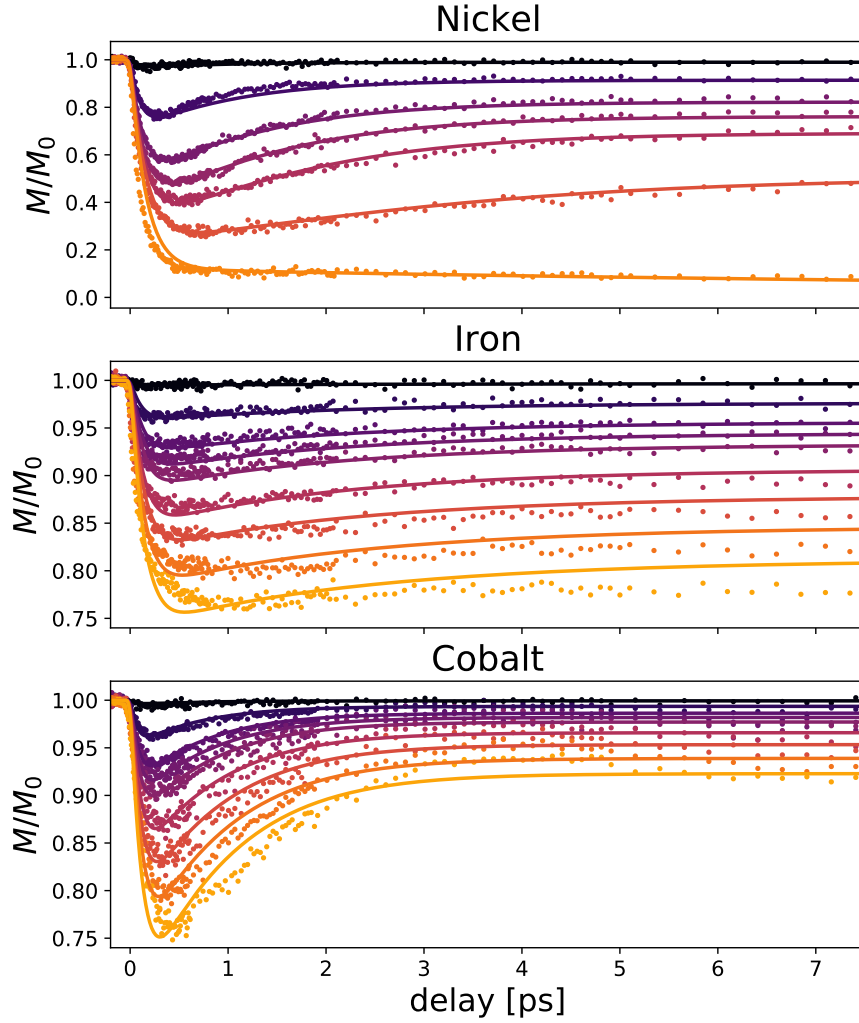


Figure 4.1: Magnetization dynamics in Nickel, Iron and Cobalt measured experimentally by Borchert et al. [31] (dots) and simulated with the extended M3TM (solid). Experiments were conducted for a set of different pump fluences, increasing from black to yellow. The corresponding values of absorbed energy are listed in table 4.1. The ratio of absorbed energies in simulations were matched to the ratio of pump fluences. To obtain the fits, the spin flip probabilities for Nickel, Iron and Cobalt were set to 0.09, 0.05 and 0.07, respectively.

yields a penetration depth $\lambda \approx 5.7$ nm, where the depth profile of both pump pulse at a given delay time reads $P(ja) = P_0 \exp\left\{-\frac{ja}{\lambda}\right\}$, where j denotes the sample layer and a is the lattice constant. Having estimated the pump laser penetration depth, the absorbed fluence in simulations can be calculated as

$$F_{a,\text{sim}} = \int_{t_0}^{\infty} d\tau \sum_{j=0}^N a P(ja, t), \quad (4.1)$$

where $Na = 15$ nm is the total sample depth and t_0 is any time before injection of the pump pulse. Equation 4.1 holds as long as heat diffusion out of the sample is neglected. While phononic heat diffusion is neglected, electronic heat diffusion was respected in terms of the continuity equation 2.37. Since the samples were grown on insulating substrates, there is no diffusion to this end. For simplicity, also the coupling of the cap and sample was neglected here, so that heat diffusion was treated only internally. The influence of a layer-resolved treatment of the sample in simulations on the magnetization dynamics was also tested. Since the magnetization is no longer uniform within the sample upon respecting exponential decay of the pump pulse and heat diffusion, a Kerr signal was calculated with an exponential response of the probe pulse as well:

$$m_{\text{kerr}}(t) = \sum_{i=0}^N a m(i, t) \exp\left\{-\frac{i a}{\lambda}\right\} \quad (4.2)$$

To this end, the same penetration depth was chosen for the probe pulse as for the pump pulse, since it has been reported that the magnetic response for probe pulses of 400 nm and 800 nm does not deviate significantly [32]. It was found that the influence of layer resolved simulations are very minor. Indeed, the spin-flip probability was chosen identically in both methods and both the depth and delay of the demagnetization peak are identical in both

approaches. The difference in absorbed fluences in simulations for Nickel and Iron/Cobalt for equal experimental incident fluences could be due to different reflective or absorption properties. Note that conventional M3TM simulations would predict smaller absorbed energies, as explained in section 3.4. Figure 4.1 shows the experimental data and simulated fits for Iron, Nickel and Cobalt upon treating the sample uniformly in simulations. In order to fit the data for all fluences, an intermediate fluence of $5 \frac{\text{mJ}}{\text{cm}^2}$ was chosen to fix P_0 and thus the absorbed energy for all fluences. Across all samples, the best fits could be obtained by setting $\sigma = 18$ fs. The fits will be discussed in the following subsections.

experimental		simulated			
incident fluence $[\frac{\text{mJ}}{\text{cm}^2}]$	absorbed fluence $[\frac{\text{mJ}}{\text{cm}^2}]$	$P_0^* [10^{21} \frac{\text{W}}{\text{m}^2}]$		absorbed fluence $[\frac{\text{mJ}}{\text{cm}^2}]$	
		Nickel	Iron/Cobalt	Nickel	Iron/Cobalt
0.5		1.68	1.33	0.11	0.09
3		10.1	8	0.68	0.54
5		16.8	13.3	1.125	0.9
6		20.3	16	1.35	1.06
7		23.7	18.6	1.58	1.23
9	4.1 [31]	30.5	23.9	2.03	1.59
11		38.5	29	2.48	1.87
13			34.2		2.34
15			39.4		2.78

Table 4.1: Table of the experimental incident pump fluences and estimated absorbed fluences as explained in the text. These are compared to the pump powers P_0^* for monolayer calculations and the absorbed fluences in layer resolved simulations. Note that the ratio of fluences is very well reflected by both the absorbed fluences and peak pump power densities used in simulations. The experimentally determined absorbed fluence for $F_{i,exp} = 4 \frac{\text{mJ}}{\text{cm}^2}$ however is twice as high as the simulated absorbed fluence.

parameter	Nickel	Iron	fcc-Cobalt
T_C [K]	631 [34]	1043 [34]	1388 [34]
T_D [K]	345 [35]	373 [35]	386 [35]
μ_{at} [μ_B]	0.6 [36]	2.2 [36]	1.7 [36]
a [Å]	3.52 [37]	2.87 [37]	3.55 [38]

Table 4.2: List of parameters used in simulations shown in Fig. 4.1.

4.1.1 Nickel

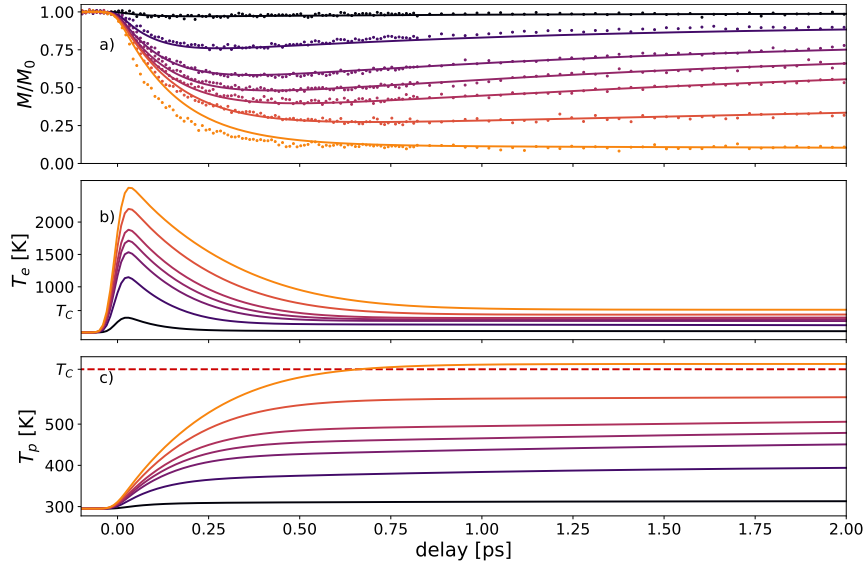


Figure 4.2: Dynamics of a) magnetization, b) electron temperature and c) phonon temperature for Nickel. The dots show experimental data from Borchert et al. [31].

Out of the three investigated transition metals, Nickel has the lowest atomic magnetic moment μ_{at} and thus the lowest Curie temperature T_C (see Tab. 4.2). Both these parameters effectively increase the magnetization dynamics rate (see equation 2.40), as the rate parameter R scales linearly as $\frac{1}{\mu_{\text{at}}}$ and equilibrium magnetization for a given electron temperature is lower the lower

T_c . With the spin-flip probabilities being in the same order of magnitude across the three transition metals, the M3TM predicts that Nickel shows the largest demagnetization out of them. This feature is reflected in the experimental data. Overall, the simulations match experimental data very well. For all fluences the final magnetization, as well as depth and delay of the demagnetization phase match perfectly between theory and experiment. The spin-flip probability was set to $a_{\text{sf}} = 0.09$ for all simulations, which matches the predictions of $a_{\text{sf}} = 0.09$ for non thermal electron distributions of Carva et al..

4.1.2 Iron

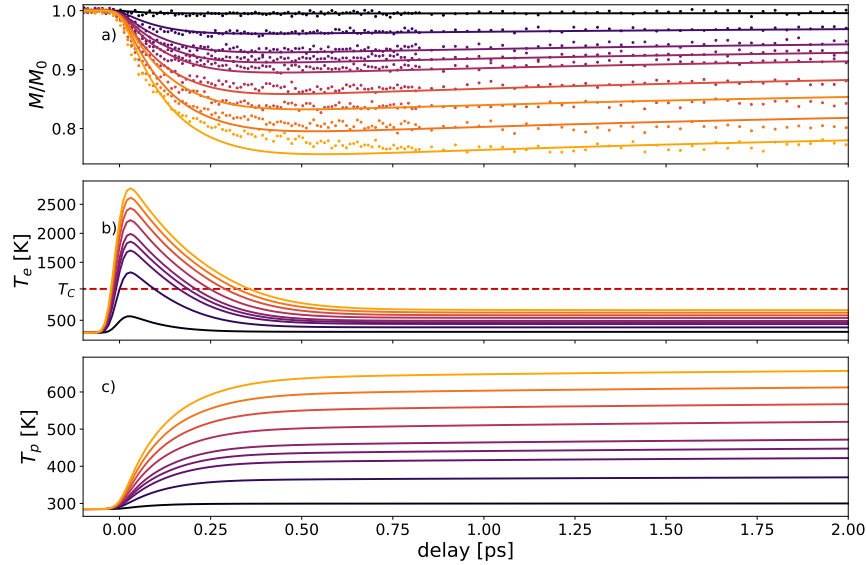


Figure 4.3: Dynamics of a) magnetization, b) electron temperature and c) phonon temperature for Iron. The dots show experimental data from Borchert et al. [31].

As shown in figure 3.9 ab initio calculations predict Iron to have the lowest lattice heat capacity of the three investigated materials. As explained in section 3.2.3 this translates into little remagnetization on the timescale of

electron-phonon equilibration. Experimental data shows the expected behaviour. Simulations fit very well in the low to mid fluence regime. From incident fluences of $11 \frac{\text{mJ}}{\text{cm}^2}$ however, the final magnetization is higher than observed experimentally and the magnetization peaks later than predicted by simulations. The latter effect has been studied in a similar setup of double pump experiments on Iron, where it was found that demagnetization is significantly slowed down for hot electron distributions [39]. While only a single pump of short duration is used in this experiment, nonlinear effects can come into play for high fluences. Higher order perturbation theory may be needed to describe the transition rates, which are merely calculated from Fermi's golden rule in the M3TM.

Comparing the data sets on Iron from Borchert [31] and Carpine [3] (shown in Fig. 2.4), the data deviates significantly. The samples measured by Carpine demagnetize stronger upon irradiation with a pump pulse of the same fluence, which is probably due to different reflective properties of the samples. More striking is different behaviour in the remagnetization phase. While the Carpine's data suggests that the sample significantly remagnetizes, the data shown here shows little to no remagnetization on the same timescale. As will be discussed in the next section, the retrieved magnetization dynamics depend strongly on interpretation of raw MOKE data.

The simulations were conducted with a spin-flip probability of $a_{\text{sf}} = 0.05$, which is again well within the range $a_{\text{sf}} = 0.04 - 0.09$ predicted by Carva et al. [5].

4.1.3 Cobalt

As for the data on the magnetization dynamics in Iron, for Cobalt very good fits were obtained for intermediate fluences of $3 - 9 \frac{\text{mJ}}{\text{cm}^2}$. In the demagnetization phase the data resembles the behaviour of Iron, which can be understood in terms of similar magnetization rate parameters R and similar Curie temperatures. Due to higher lattice specific heat of Cobalt, the M3TM predicts a stronger remagnetization, which fits nicely to experimental data.

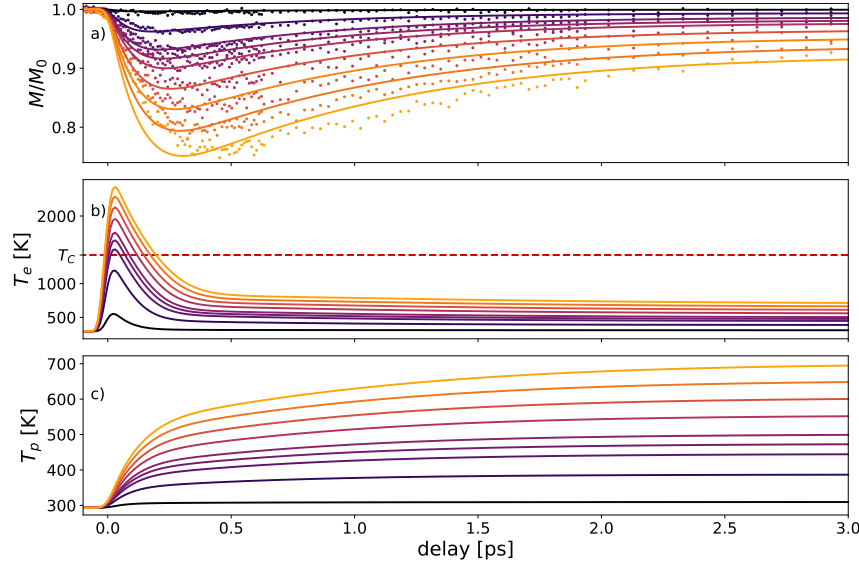


Figure 4.4: Dynamics of a) magnetization, b) electron temperature and c) phonon temperature for Cobalt. The dots show experimental data from Borchert et al. [31].

The fits have been obtained with spin-flip probability $a_{\text{sf}} = 0.07$, which is significantly larger than predicted by Carva et al. ($a_{\text{sf}} = 0.01 - 0.022$).

4.2 Data collected from Kerr rotation and ellipticity

The second data set to be discussed was kindly provided by Chekhov et al. from the AG Kampfrath at the FU Berlin, who recovered magnetization dynamics on an Iron sample of approximately 7 nm thickness [32]. They used MOKE technique in a pump probe configuration with optical as well as THz laser excitation and measured both the Kerr rotation and the Kerr ellipticity of the reflected probe pulse. Each signal $S^{(r)}(t)$ at delay t after pump excitation is linear in the magnetization $m(t)$ in the sense

$$S^{e(r)}(t) = a^{e(r)}(t)m(t) + b^{e(r)}(t). \quad (4.3)$$

For optical excitation, the first term is proportional to the in plane magnetization and the second term is a non magnetic contribution due to different Fresnel coefficients for s- and p- polarization of the incident probe pulse. Both the magnetic response $a^{e(r)}(t) = \frac{\partial S^{e(r)}}{\partial m}$ and the nonmagnetic contribution $b^{e(r)}(t)$ are time dependent. They can be distinguished by measuring the signal transients

$$\Delta S^{e(r)} = \Delta a^{e(r)} m + a^{e(r)} \Delta m + \Delta b^{e(r)} \quad (4.4)$$

for both positive and negative initial magnetization $\pm m_0$ and subtracting them, since the first term in equation 4.4 is odd upon switching the initial magnetization while the second term is even. This yields $\Delta S_{\pm m}(t) = \Delta S^{e(r)}(+m_0) - \Delta S^{e(r)}(-m_0)$, which due to different dynamics of the responses $a^{e(r)}(t)$ deviates for ellipticity (e) and rotation (r), as shown in figure 4.5a).

Using the normalized even response transients

$$\begin{aligned} \delta m &= \frac{2\Delta S_{\pm m}^{e(r)}}{S_{\pm m}(t=0)} \\ &= \frac{\Delta m}{m_0} + \frac{\Delta a^{e(r)}}{a_0^{e(r)}} \end{aligned} \quad (4.5)$$

and assuming a linear relation between the response functions $\Delta a^r = g\Delta a^e$, the magnetization dynamics can be calculated by the simple relation

$$\delta m(t) = \frac{\delta S^r(t) - g\delta S^e(t)}{1 - g} \quad (4.6)$$

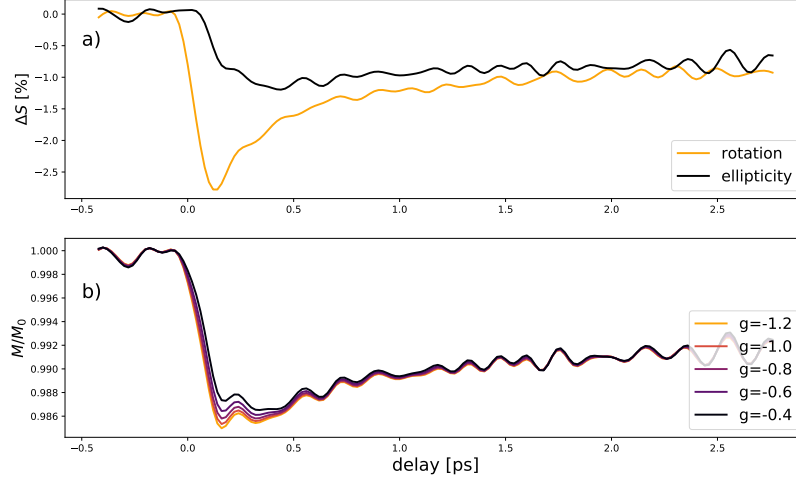


Figure 4.5: a) MOKE signal transient ΔS of Kerr ellipticity and rotation measured of an 7 nm Iron sample upon irradiation with an optical pump pulse of low fluence below $0.1 \frac{\text{mJ}}{\text{m}^2\text{K}}$. Rotation measurements suggest both quicker and a more drastic magnetization quenching than the response of the Kerr ellipticity. b) Magnetization dynamics calculated from rotation/ellipticity data and equation 4.6 for different values of g . Both the amount and delay of full magnetization quenching is influenced by different proportionality constants of ellipticity- and rotation-responses.

The extracted magnetization dynamics then depend on normalization of the data (fixation of M_0) and the choice of the constant g , whose influence is shown in figure 4.5b). Due to the different responses of rotation and ellipticity within the first few hundred fs, not only the amount of magnetization quenching is influenced by weighting the signals through the factor g , but also the delay of the demagnetization peak shifts.

Figure 4.6 shows magnetization dynamics computed with equation 4.6 for different g -values and fits obtained with extended M3TM simulations. The dynamics with $g = -1$ suggest stronger quenching of magnetization and

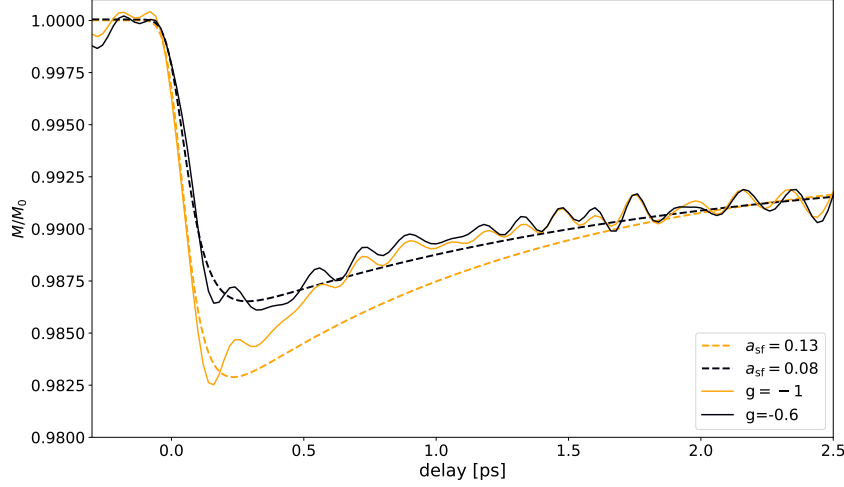


Figure 4.6: Magnetization dynamics retrieved from experimental data (see figure 4.5a)) and different g -values (solid lines), as well as fits computed with the extended M3TM and different values for the spin flip probability a_{sf} .

thus the spin flip probability a_{sf} was increased to match the depth of the demagnetization peak. The simulation does not fit the remagnetization phase well. As can be seen in section 3.2.2, higher electron-phonon coupling would be needed to account for the rapid remagnetization properly. Choosing $g = -0.6$ not only decreases the apparent magnetization quenching, but also shifts the peak to slightly later delay times. In this case, simulations with a smaller magnetization rate recover the experimental data very nicely. The value of $a_{\text{sf}} = 0.08$ again falls within the range predicted by Carva et al. for non thermal electron distributions right after laser excitation [5]. The value for g should be retrieved from requiring no discontinuities before delay $t = 0$. However, deviations in the magnetization dynamics for different values of g at times $t < 0$ are much smaller than the signal noise, so that an exact determination of g is precarious. Altogether it can be seen that treatment of raw experimental data has significant influence on the quality

of simulation fits. Selecting $g = -0.6$ the experimental data can be reproduced by the extended M3TM with the same parameters used for the data provided by Borchert et al. [31].

Chapter 5

Conclusion

In this thesis, ultrafast magnetization dynamics upon optical laser excitation was studied by the means of the Microscopic Three Temperature Model. Therefor, a simulation code was written to calculate the dynamics of the electronic, phononic and spin subsystems. The motivation to revisit the M3TM, which was already proposed in 2009 by Koopmans and co-workers [2], is the debate about the magnitude of the spin-flip probability upon an electron phonon scattering event. As introduced in section 2.2.5, Carva et al. developed a method to compute the spin-flip probability within relativistic Density functional theory calculations [5]. To retrieve a value for spin-flip probability from simulations, as many simulation parameters as possible have to be fixed. Thus, temperature dependent ab initio calculations for the specific heats of the electron and phonon systems as well as the rate of energy transfer between the two have been implemented. These parameters were calculated by Jan Vorbergers group at the Helmholtz Zentrum Dresden-Rossendorf [6] using Density functional theory. After introducing the analytical model and derivation of the M3TM and comparing it to other proposed spin-flip mechanisms in section 2.2, the influence of the parameters for pump pulse, electron-phonon-dynamics and response of the spin system on the magnetization dynamics were discussed in section 3.2. Com-

paring *ab initio* parameters with the fit values used by Koopmans et al. [2] showed that an overestimation of the electronic heat capacity yields an overestimation of the spin-flip probability in fitting simulations to experimental data. In this thesis, as a small extension to the M3TM, a term allowing for energy transfer between electron- and spin- subsystems was introduced to account for spin specific heat. The term originates in the mean field Heisenberg model and was introduced in section 3.4. In section 4 two experimental data sets were discussed. Magnetization dynamics retrieved from MOKE measurements for a set of incident pump fluences on Iron, Nickel and Cobalt were conducted by Borchert et al. [31] at the Max-Born-Institute for nonlinear optics in Berlin. Since the ratio of incident pump fluences should be reflected in the ratio of simulated pump fluences, assuming a linear behaviour of incidence and absorption, the spin-flip probability is the only free parameter in the simulations. It was shown that the extended M3TM with the implemented parameters is capable to reproduce the magnetization dynamics measured for all Iron, Nickel and Cobalt very well. Especially for the lowest six fluences up to $11 \frac{\text{mJ}}{\text{cm}^2}$, the experimental data was reproduced very well by simulations. The estimated absorbed fluences from experiments were compared to layer-resolved simulations with non-uniform pulse absorption and temperature dynamics and show reasonable agreement. The extracted spin-flip probabilities for Iron and Nickel are in good agreement to the *ab initio* calculations from Carva et al., whereas values for Cobalt exceed theoretical predictions, while being significantly lower than predicted by Koopmans et al. A second data set on magnetization dynamics in Iron stems from Chekhov et al. in a collaboration of the FU Berlin and The University of Greifswald. They recorded data on Kerr ellipticity and rotation and retrieved magnetization dynamics from weighing the signals differently. It was shown that a possible fit between simulation and experiment is highly sensitive to the the weights given to rotation and ellipticity. At the same time, determining the correct treatment of experimental data is difficult due to noise.

Altogether, it was shown that the M3TM can very well reproduce critical features of ultrafast magnetization dynamics upon optical laser excitation. Fitting simulations to experimental data from three different materials under the same conditions yielded very good results and the spin-flip probability needed to fit the data was found to be much smaller than predicted by Koopmans et al. [2] and are within the range predicted by ab initio calculations [5].

Bibliography

- [1] E. Beaurepaire, J.-C. Merle, A. Daunois, and J.-Y. Bigot. Ultrafast spin dynamics in ferromagnetic nickel. *Phys. Rev. Lett.*, 76:4250–4253, May 1996.
- [2] B. Koopmans, G. Malinowski, F. Dalla Longa, D. Steiauf, M. Fähnle, T. Roth, M. Cinchetti, and M. Aeschlimann. Explaining the paradoxical diversity of ultrafast laser-induced demagnetization. *Nature Materials*, 9(3):259–265, 2010.
- [3] E. Carpena, E. Mancini, C. Dallera, M. Brenna, E. Puppini, and S. De Silvestri. Dynamics of electron-magnon interaction and ultrafast demagnetization in thin iron films. *Phys. Rev. B*, 78:174422, Nov 2008.
- [4] Michael Krauß, Tobias Roth, Sabine Alebrand, Daniel Steil, Mirko Cinchetti, Martin Aeschlimann, and Hans Christian Schneider. Ultrafast demagnetization of ferromagnetic transition metals: The role of the coulomb interaction. *Phys. Rev. B*, 80:180407, Nov 2009.
- [5] Ritwik Mondal, Marco Berritta, Karel Carva, and Peter M. Oppeneer. Ab initio investigation of light-induced relativistic spin-flip effects in magneto-optics. *Physical Review B*, 91(17), May 2015.
- [6] Daniela Zahn, Florian Jakobs, Yoav William Windsor, Hélène Seiler, Thomas Vasileiadis, Tim A. Butcher, Yingpeng Qi, Dieter Engel, Unai

- Atxitia, Jan Vorberger, and Ralph Ernstorfer. Lattice dynamics and ultrafast energy flow between electrons, spins, and phonons in a 3d ferromagnet. *Phys. Rev. Research*, 3:023032, Apr 2021.
- [7] U. Atxitia and O. Chubykalo-Fesenko. Ultrafast magnetization dynamics rates within the landau-lifshitz-bloch model. *Phys. Rev. B*, 84:144414, Oct 2011.
- [8] S. D. Brorson, A. Kazeroonian, J. S. Moodera, D. W. Face, T. K. Cheng, E. P. Ippen, M. S. Dresselhaus, and G. Dresselhaus. Femtosecond room-temperature measurement of the electron-phonon coupling constant γ in metallic superconductors. *Phys. Rev. Lett.*, 64:2172–2175, Apr 1990.
- [9] MB Agranat, SI Ashitkov, AB Granovskii, and GI Rukman. Interaction of picosecond laser pulses with the electron, spin, and phonon subsystems of nickel. *Zh. Eksp. Teor. Fiz*, 86(1376):10, 1984.
- [10] N. Kazantseva, U. Nowak, R. W. Chantrell, J. Hohlfeld, and A. Rebei. Slow recovery of the magnetisation after a sub-picosecond heat pulse. *EPL (Europhysics Letters)*, 81(2):27004, dec 2007.
- [11] H.-S. Rhie, H. A. Dürr, and W. Eberhardt. Femtosecond electron and spin dynamics in Ni/W(110) films. *Phys. Rev. Lett.*, 90:247201, Jun 2003.
- [12] Zhibin Lin, Leonid V. Zhigilei, and Vittorio Celli. Electron-phonon coupling and electron heat capacity of metals under conditions of strong electron-phonon nonequilibrium. *Phys. Rev. B*, 77:075133, Feb 2008.
- [13] G. R. Stewart. Measurement of low-temperature specific heat. *Review of Scientific Instruments*, 54(1):1–11, 1983.
- [14] D. A. Garanin. Fokker-planck and landau-lifshitz-bloch equations for classical ferromagnets. *Physical Review B*, 55(5):3050–3057, Feb 1997.

- [15] U Atxitia, D Hinzke, and U Nowak. Fundamentals and applications of the landau–lifshitz–bloch equation. *Journal of Physics D: Applied Physics*, 50(3):033003, dec 2016.
- [16] R. J. Elliott. Theory of the effect of spin-orbit coupling on magnetic resonance in some semiconductors. *Phys. Rev.*, 96:266–279, Oct 1954.
- [17] W. Kuch. Magnetic dichroism study of the relativistic electronic structure of perpendicularly magnetized ni/cu(001). *Journal of applied physics*, 79, Aug 1996.
- [18] Y. Yafet. g factors and spin-lattice relaxation of conduction electrons**part of the work connected with the preparation of this article, in particular the work on spin-lattice relaxation, was done while the author was at the westinghouse research laboratories, pittsburgh, pennsylvania. In Frederick Seitz and David Turnbull, editors, *Solid State Physics vol.14*, volume 14 of *Solid State Physics*, pages 1–98. Academic Press, 1963.
- [19] J. Fabian and S. Das Sarma. Spin relaxation of conduction electrons in polyvalent metals: Theory and a realistic calculation. *Phys. Rev. Lett.*, 81:5624–5627, Dec 1998.
- [20] Andrei Kirilyuk, Alexey V. Kimel, and Theo Rasing. Ultrafast optical manipulation of magnetic order. *Rev. Mod. Phys.*, 82:2731–2784, Sep 2010.
- [21] AJ Schellekens. *Manipulating spins : novel methods for controlling magnetization dynamics on the ultimate timescale*. PhD thesis, Eindhoven University of Technology, 1 2014.
- [22] A. Kozhevnikov, Alexey Lukoyanov, Viadimir Anisimov, and M. Korotin. Transition of iron ions from high-spin to low-spin state and pressure-induced insulator-metal transition in hematite fe₂o₃. *Journal of Experimental and Theoretical Physics*, 105:1035–1042, 11 2007.

- [23] U Köbler, J Englich, O Hupe, and J Hesse. Effective spin quantum numbers in iron, cobalt and nickel. *Physica B: Condensed Matter*, 339(4):156–163, 2003.
- [24] M. Beens, M. L. M. Lalieu, A. J. M. Deenen, R. A. Duine, and B. Koopmans. Comparing all-optical switching in synthetic-ferrimagnetic multilayers and alloys. *Phys. Rev. B*, 100:220409, Dec 2019.
- [25] F. Beuneu and P. Monod. The elliott relation in pure metals. *Phys. Rev. B*, 18:2422–2425, Sep 1978.
- [26] P. Monod and F. Beuneu. Conduction-electron spin flip by phonons in metals: Analysis of experimental data. *Phys. Rev. B*, 19:911–916, Jan 1979.
- [27] Philip B. Allen. Theory of thermal relaxation of electrons in metals. *Phys. Rev. Lett.*, 59:1460–1463, Sep 1987.
- [28] C. Boeglin, E Beaurepaire, V. Halté, V López-Flores, Christian Stamm, Niko Pontius, Hermann Durr, and Jean-Yves Bigot. Distinguishing the ultrafast dynamics of spin and orbital moments in solids. *Nature*, 465:458–61, 05 2010.
- [29] Zhibin Lin, Leonid V. Zhigilei, and Vittorio Celli. Electron-phonon coupling and electron heat capacity of metals under conditions of strong electron-phonon nonequilibrium. *Phys. Rev. B*, 77:075133, Feb 2008.
- [30] Peter J. Meschter, James W. Wright, Charlie R. Brooks, and Thomas G. Kollie. Physical contributions to the heat capacity of nickel. *Journal of Physics and Chemistry of Solids*, 42(9):861–871, 1981.
- [31] Martin Borchert, Clemens Schmising, Daniel Schick, Dieter Engel, Sangeeta Sharma, and Stefan Eisebitt. Manipulation of ultrafast demagnetization dynamics by optically induced intersite spin transfer in magnetic compounds with distinct density of states. 08 2020.

- [32] Alexander Chekhov, Y. Behovits, J. Heitz, Christian Denker, D. Reiss, M. Wolf, M. Weinelt, P. Brouwer, Markus Münzenberg, and Tobias Kampfrath. Ultrafast demagnetization of iron induced by optical vs terahertz pulses. 06 2021.
- [33] J. Gütde, J. Hohlfeld, J.G. Müller, and E. Matthias. Damage threshold dependence on electron–phonon coupling in au and ni films. *Applied Surface Science*, 127-129:40–45, 1998.
- [34] P Mohn and E P Wohlfarth. The curie temperature of the ferromagnetic transition metals and their compounds. *Journal of Physics F: Metal Physics*, 17(12):2421–2430, dec 1987.
- [35] C Y Ho, R W Powell, and P E Liley. Thermal conductivity of the elements: a comprehensive review. *J. Phys. Chem. Ref. Data, Suppl.*, v. 3, no. 1, pp. 1-796, 12 1974.
- [36] Stefan Blügel. C 1 reduced dimensions i : Magnetic moment and magnetic structure. 2005.
- [37] Wheeler P. Davey. Precision measurements of the lattice constants of twelve common metals. *Phys. Rev.*, 25:753–761, Jun 1925.
- [38] J R Cerda, P L de Andres, A Cebollada, R Miranda, E Navas, P Schuster, C M Schneider, and J Kirschner. Epitaxial growth of cobalt films on cu(100): a crystallographic LEED determination. *Journal of Physics: Condensed Matter*, 5(14):2055–2062, apr 1993.
- [39] Kevin Bühlmann, Rafael Gort, Gerard Salvatella, Simon Däster, Andreas Fognini, Thomas Bähler, Christian Dornes, C. A. F. Vaz, Andreas Vaterlaus, and Yves Acremann. Ultrafast demagnetization in iron: Separating effects by their nonlinearity. *Structural Dynamics*, 5(4):044502, 2018.
- [40] Jacob Schliesser and Brian Woodfield. Development of a debye heat capacity model for vibrational modes with a gap in the density of states.

Journal of physics. Condensed matter : an Institute of Physics journal,
27:285402, 06 2015.

- [41] A. L. Chekhov, Y. Behovits, J. J. F. Heitz, C. Denker, D. A. Reiss, M. Wolf, M. Weinelt, P. W. Brouwer, M. Münzenberg, and T. Kampfrath. Ultrafast demagnetization of iron induced by optical vs terahertz pulses, 2021.

Eidesstattliche Erklärung

Hiermit versichere ich,

Vorname

Name

Matrikelnummer

geboren am

geboren in

,

an Eides statt, dass die vorliegende Arbeit von mir selbstständig und ohne unerlaubte Hilfe Dritter verfasst wurde und ich keine anderen als die angegebenen Quellen und Hilfsmittel verwendet sowie wörtliche und sinngemäße Zitate als solche kenntlich gemacht habe.

Diese Arbeit hat in gleicher oder ähnlicher Form noch keiner anderen Prüfungsbehörde vorgelegen und wurde bisher nicht veröffentlicht.

Ort, Datum

Unterschrift

Danksagung

Ich weiß nicht, ob eine Danksagung oder Widmung für eine Masterarbeit angebracht ist. Ich weiß aber auch nicht, ob ich noch einmal die Chance bekomme, eine akademische Arbeit zu veröffentlichen. Daher möchte ich diese Arbeit meinem Papa Tobias Gripe widmen. Papa war sich ziemlich früh sicher, dass ich das Studium hier abschließen würde, lange bevor ich mir das selber zugetraut habe. Ich hätte noch eine Menge von ihm zu lernen gehabt, zum Beispiel welcher nun der Diminuend und welcher der Subtrahent ist. Tut mir Leid, aber das konnte ich mir nie merken. Papa war ein bescheidener Mann und hat oft Bewunderung dafür ausgesprochen, dass ich mich mit so etwas wie Physik auseinandersetzen kann. Ingeheim wusste er aber hoffentlich, dass es viel bewundernswerter ist, eine siebenköpfige Familie voller Chaoten so liebevoll zu finanzieren und zu organisieren, wie er es immer gemacht hat. Danke.

Dank auch an Unai, der mich gut betreut hat, obwohl wir nie im Büro bei-/ und miteinander arbeiten konnten. Desweiteren danke ich Florian Jakobs für die Bereitstellung seiner Simulationsdaten und Hilfe bei deren Interpretation, sowie der Arbeitsgruppe von Tobias Kampfrath, und Martin Borchert für die Bereitstellung ihrer experimentellen Datensätze. Danke an Manu, Nico und Alex für interessante Gespräche über Physik jeder Art. Ohne kritische Nachfragen und Diskussionen zu dieser Arbeit hätte ich ein flacheres Verständnis von dem, was ich hier behandelt habe. Vor allem aber danke für die schönen Zeiten, die wir verbringen, ohne an Physik zu denken. Das gilt auch für Mama, Dele, Elsi, Jonni und Otto, die mich immer aufgefangen haben, wenn ich gestresst war und auf andere Gedanken kommen musste.